IN-45-CR

79980

P.57

Semi-annual report for NASA Grant NAG5-1125 entitled

"The Role of Global Cloud Climatologies in Validating Numerical Models"

Principal Investigator: Harshvardhan
Department of Earth and Atmospheric Sciences
Purdue University
West Lafayette, Indiana 47907

October 1, 1991 - March 31, 1992

The grant period covered in this report was devoted to the study of radiative transfer approximations in collaboration with Dr. Michael King of NASA/Goddard Space Flight Center. A manuscript describing the study has been submitted for publication to the *Journal of the Atmospheric Sciences*. A copy is being attached for your records.

In addition the prior study on surface longwave fluxes derived using a hybrid method (reported earlier) has been re-submitted after revisions to the *Journal of Climate*. The revised manuscript is also attached for your records.

As part of the ongoing research project we have now acquired a continuous record of ISCCP C-1 data extending from October 1, 1985 - April 30, 1989. This extensive cloud data set will be used in future studies including efforts in collaboration with personnel in the Radiation and Climate Branch of NASA/Goddard Space Flight Center.

Some ongoing research results will be presented at the AGU Spring meeting in Montreal, May 11-16. The titles of two presentations to be made at the meeting are:

1. The application of similarity relations to the computation of spectrally integrated solar absorption by water clouds by Harshvardhan and Michael D. King (NASA/Goddard).
2. A spectral investigation of the atmospheric shortwave cloud radiative forcing by William L. Ridgway (ARC; NASA/Goddard) and Harshvardhan.

CLOUD RADIATIVE FORCING AND THE SURFACE LONGWAVE RADIATION

Hui Zhi and Harshvardhan

Department of Earth and Atmospheric Sciences
Purdue University
West Lafayette, IN 47907

Abstract

Global maps of the monthly mean net upward longwave radiation flux at the ocean surface have been obtained for April, July, October 1985 and January 1986. These maps were produced by blending information obtained from a combination of general circulation model cloud radiative forcing fields, the top-of-the-atmosphere cloud radiative forcing from ERBE and TOVS profiles and sea surface temperature on ISCCP C1 tapes. The fields are compatible with known meteorological regimes of atmospheric water vapor content and cloudiness. There is a vast area of high net upward longwave radiation flux (> 80 Wm^{-2}) in the eastern Pacific Ocean throughout most of the year. Areas of low net upward longwave radiation flux (<40 Wm^{-2}) are the tropical convective regions and extra tropical regions that tend to have persistent low cloud cover. The technique used in this study relies on GCM simulations and so is subject to some of the uncertainties associated with the model. However, all input information regarding temperature, moisture and cloud cover is from satellite data having near global coverage. This feature of the procedure alone warrants its consideration for further use in compiling global maps of the net longwave radiation at the surface, at least over the oceans.

1. Introduction

The surface radiation budget, i.e., the net solar radiation absorbed minus the net longwave radiation emitted, and its spatial and temporal variations are key parameters in climate and weather studies. This budget plays a major role in determining radiative heating, as well as sensible and latent heat fluxes over ocean and land surfaces. As a result, the net radiative flux constitutes an important boundary forcing for the general ocean circulation and a crucial parameter for determining meridional oceanic heat transport, ocean-atmosphere interaction and land-atmosphere interaction. Moreover, it is a useful parameter when addressing issues related to climate change due to CO_2 and other trace gases, and in the validation of radiation schemes used in climate models. Therefore, it is understandable for the atmospheric and oceanic communities to need reliable estimates of the surface radiation budget (WCP-92 1984).

Direct high-quality radiation measurements at the surface are difficult to make, particularly over the oceans which cover more than 60% of the Earth's surface. Actually there are very few surface stations measuring the radiation budget routinely and reliably because of the requirement of careful instrument calibration and temperature correction for the radiation, especially longwave, measurement. In addition, because of operating costs, it is not feasible to maintain a network of surface stations over the oceans. Although an attempt has been made to use ships to observe some meteorological parameters such as sea surface temperature, air temperature, specific humidity near the surface and even fractional cloud coverage, there has not been much progress in the measurement of surface radiation. Few ships measure radiation quantities because of special needs that require a dedicated facility for this purpose. Moreover, regular ship observations are limited along commercial shipping lanes, and vast geographic gaps still exist, especially in the southern hemisphere. Consequently, the empirical formulas used to derive budgets have been validated only over limited regions, and when applied globally, large errors are inevitable. Therefore, direct measurement of shortwave and longwave radiation fluxes at the surface globally has not been possible.

Since there are difficulties in obtaining radiative data from surface stations routinely and reliably, it has been realized that space based observations are the only means to have global coverage. However, because of the intervening atmosphere, the surface radiation budget is difficult to measure from satellites, whereas the top-of-the-atmosphere (TOA) radiation balance can be measured directly. Over the past decades, considerable effort has been expended in the global measurement of the TOA radiation budget. Attempts at inferring the surface radiation budget from space based measurements have only begun recently.

There has been some success in obtaining the solar radiation budget at the surface (e.g. Raschke and Preuss 1979; Tarpley 1979; Gautier et al. 1980; Pinker and Ewing 1985; Justus et

al. 1986). The progress in surface longwave radiation budget measurements from space, however, has been much slower. Currently, some techniques are available to estimate the downward longwave component of the surface flux (Darnell et al. 1983, 1986; Chou 1985; Schmetz et al. 1986; Frouin et al. 1988; Ardanuy et al. 1989; Wu and Cheng 1989; Breon et al. 1991). The net longwave component at the surface can be estimated by the difference between the upwelling and downwelling fluxes. The upward component is determined directly from sea surface temperature since the oceanic surface emits essentially as a blackbody. The downward flux, however, is more difficult to obtain since it depends on many meteorological parameters such as atmospheric moisture, temperature and cloud cover. Because of the uncertainty of the measurement of these meteorological parameters, at present there is a need for improvement in the estimation of net longwave radiation fluxes at the surface.

Two types of methods have been used to estimate the downward longwave flux at the surface: statistical and physical. As the name implies, statistical methods rely on correlations between fluxes and observed meteorological parameters. The physical techniques are based on modeling radiative processes occurring in the atmosphere (clear and cloudy atmosphere). The downward flux is computed from radiative transfer models which utilize parameters obtained from satellite radiance data. These parameters include temperature and water vapor mixing ratio profiles, fraction of cloud coverage and cloud emittance. However, all physical methods currently under consideration have to make certain assumptions regarding both the presence of clouds and their vertical extent. Recent examples of these attempts are Chou (1985), Schmetz et al. (1986), Darnell et al. (1986), Gupta (1989), and Wu and Cheng (1989). The treatment of longwave radiation transmittance in the presence of clouds becomes more complex since knowledge of cloud top and base heights and emittances are required. For this reason, it is important to determine the vertical profile of cloudiness as well as the horizontal distribution of clouds and associated emittances. Unfortunately, determination of the vertical profile of cloudiness from space based measurements is difficult since overlap of cloudy layers is common in the real atmosphere. Therefore, because of the uncertainties in assumed cloudiness, all these methods often give unreliable results.

The method used here to obtain monthly mean quantities avoids the explicit computation of cloud fraction and the location of cloud base in estimating the downward longwave radiation globally (Harshvardhan et al. 1990). An advantage of this technique is that no independent knowledge or assumptions regarding cloud cover for a particular month are required. The only information required is a relationship between the cloud radiative forcing (CRF) at the top of the atmosphere and that at the surface, which is obtained from a general circulation model (GCM) simulation.

2. Method

The cloud radiative forcing (CRF) has been defined as the difference between the radiative flux as measured or computed and the clear sky flux (Charlock and Ramanathan 1985; Ramanathan 1987). For example, the longwave cloud radiative forcing at the surface is

Surface LWCRF = Surface LW Flux - Clear Sky Surface LW Flux. (1)

Previous studies have shown that there is no correlation between the spectrally integrated outgoing longwave radiation and the net longwave at the surface (Ramanathan 1986; Weare 1989). But Harshvardhan et al. (1990) have recently come to the conclusion that there is a relationship between the longwave CRF at the top of the atmosphere and the surface in model simulations. This relationship has been explained on the grounds that clouds of a certain type tend to form preferentially over certain geographic areas. The technique proposed by Harshvardhan et al. (1990) to estimate surface longwave fluxes starts with the GCM simulated climatological ratio of the CRF at the top and at the surface along with the longwave CRF at the top of the atmosphere obtained from the Earth Radiation Budget Experiment (ERBE; Ramanathan 1987) to compute the surface longwave CRF for the particular month. In this way, no independent knowledge or assumptions about cloud cover are involved, thus avoiding the most uncertain step in other methods of estimating the longwave radiation budget at the surface. The next step in the procedure is to obtain an estimate of the clear sky downward longwave flux and upward emission at the surface.

As mentioned before, the downwelling longwave radiation at the surface can not be measured directly from space, but profiles of temperature and water vapor mixing ratio in clear columns are routinely obtained from inversions of measured radiances. Most attempts to compute the downwelling longwave fluxes have relied on these retrieved profiles to furnish the flux using a radiative transfer model.

Here we show results using the once daily profile contained in the data released by the International Satellite Cloud Climatology Project (ISCCP; Rossow and Schiffer 1991). ISCCP C1 data provides a daily profile of temperature and precipitable water as well as surface temperature at a 2.5° x 2.5° horizontal resolution. This information from TOVS (Tiros Operational Vertical Sounder) is used to generate clear sky downward longwave fluxes globally and upward fluxes only over the ocean where the once-a-day sampling is acceptable. The diurnal cycle of surface temperature precludes using this technique over land. The radiation code used to compute the clear sky downward flux is the one used in the UCLA/GLA (now

CSU) GCM (Harshvardhan et al. 1989; Randall et al. 1989, 1991).

A flow diagram of the technique used to obtain surface longwave fluxes is shown in Fig. 1. Calculations start from the relationship between the longwave CRF at the top of the atmosphere and at the surface (Harshvardhan et al. 1990). Results for the months of January, April, July and October are used in this study and represent the simulated monthly characteristics of this relation over the annual cycle. The longwave CRF at the top of the atmosphere as obtained from ERBE is combined with the relationship to obtain the longwave CRF at the surface for each of the four months. Then, by means of the radiative transfer model, with input meteorological parameters such as temperature profile and water vapor mixing ratio profile and sea surface temperature from ISCCP data as well as standard ozone vertical distributions, the clear-sky downward longwave radiative flux and the clear-sky net longwave upward radiation flux at the surface are obtained. Because ozone is primarily confined to the stratosphere, its contribution to downward longwave flux is much less than that of other parameters such as water vapor in the lower atmosphere. Therefore, use of a standard ozone profile is justified.

In general, it is difficult to obtain satellite estimates of clear-sky flux that do not suffer from some cloud contamination due to a combination of subsensor resolution cloud elements and clouds that may not be detectable with the spectral intervals of the current radiometer. In this study, the clear sky fluxes are computed for the atmospheric structure under cloudy conditions, but assuming a cloud-free sky. Since the CRF at the surface and the clear-sky radiative fluxes at the surface are available, based on the definition of the CRF shown in equation (1), the actual radiative fluxes are calculated simply as the clear-sky flux plus the corresponding CRF.

3. Results

a. Longwave CRF at the Surface (global)

The mean monthly distributions of the longwave cloud radiative forcing (CRF) at the surface are presented in Fig. 2 for the months of April, July and October 1985 and January 1986. They are derived by combining the longwave CRF at the top of the atmosphere from ERBE (Harrison et al. 1990) and the ratios of the CRF at the top to that at the surface. Based on the definition in equation (1), the longwave CRF is the difference between the mean longwave flux and clear sky longwave flux for the same period. Here the longwave CRFs at the top of the atmosphere are retrieved from ERBE satellite data according to this definition. In the original ERBE data, there are a few regions in the tropics where clear sky longwave radiative fluxes at the top of the atmosphere are unavailable because of the lack of clear sky pixels during the experiment period. Therefore, an interpolation is performed to make up the missing data using

neighboring points.

There are several noteworthy features of these distributions. First, regions with small surface longwave CRF are concentrated in the tropical and the subtropical oceanic areas (Fig. 2). Surface CRF is small in the tropics because the boundary layer there is moist and radiatively opaque even for clear skies. In the central Pacific Ocean, the areas with surface longwave CRF below 20 Wm^{-2} dominate throughout the year. This is also the case for the northern and central Indian Ocean in both April 1985 and January 1986. Areas with large surface longwave CRF occur over oceanic areas southwest of Indonesia, with a maximum of more than 60 Wm^{-2} in October and more than 80 Wm^{-2} in July 1985. Both of these maxima correspond to areas of tropical convective activity. In the central Atlantic Ocean, the surface longwave CRF is below 30 Wm^{-2}.

Much larger values of surface CRFs are found over continents than over oceans during most of the year. The surface values in Eurasia and North American are more than 80 Wm^{-2} in April 1985 and 60 Wm^{-2} in both October 1985 and January 1986. Evidently, all these results correspond to persistent widespread precipitation over the continents. It is interesting to note that small surface CRFs (below 30 Wm^{-2}) emerge over most continents in July 1985. These low surface CRFs are a consequence of the large CRF ratios over continents computed from the GCM. The model includes the radiative effects of convective anvils but ignores shallow convective clouds (Harshvardhan et al. 1989). The CRF at the top is therefore quite substantial but the surface CRF is not. Thus the ratio is probably an overestimate. As mentioned later, a 100 mb error in low cloud base results in a 10 Wm^{-2} error in the downward longwave flux for complete cloud cover. If the low clouds are scattered, the error should not be significant and if the boundary layer is very moist, the sensitivity to cloud base is reduced further.

There are two continents, Africa and Australia, which always have small surface CRFs throughout the year because of their large desert and semi-arid areas. Fig. 2 shows the surface CRFs there to be often below 30 Wm^{-2}, especially in northern Africa, where the values are always below 20 Wm^{-2}. It is worthwhile noting that a persistent large surface CRF region exists in the tropical region of South America. Obviously, this results from the persistent cloud cover in this region. Over high latitude regions, some areas with the largest surface longwave CRFs are found over the region poleward of 65°S, with a maximum of 150 Wm^{-2} in July and some areas over the Arctic, with a maximum of more than 140 Wm^{-2} in October and January. Two explanations are possible for this phenomenon. Physically, it is reasonable that persistent low clouds over these regions lead to high surface longwave CRF. On the other hand, an underestimate of high cloud over the polar regions in the GCM simulation can also result in the surface longwave CRFs being somewhat unreasonably high. The latter is probably the reason

for large longwave CRFs over high latitudes in Fig. 2. Finally, areas with the average range of 30-50 Wm^{-2} dominate most mid-latitude oceanic regions of both hemispheres. This is attributable to the increase in oceanic stratus in these regions.

b. Downward Longwave Radiation Flux at the Surface (global)

Downward longwave radiative fluxes at the surface for cloud-free skies, as calculated by the radiation code in the UCLA/GLA GCM in conjunction with the input meteorological parameters from the ISCCP satellite data and U. S. standard atmosphere (COESA 1976), are presented in Fig. 3 for April, July and October 1985 and January 1986 respectively.

Over the oceanic areas, clear sky surface downward longwave fluxes have pronounced zonal distributions, especially in mid-latitudes and near polar regions. In the tropical and subtropical areas, the regions with large downward fluxes (larger than 400 Wm^{-2}) are centered over Southeast Asia in April and October 1985 and shift a little northward in July 1985 and, as expected, a little southward in January 1986. This is not surprising since the surface downward longwave fluxes for clear skies are related closely with seasonal changes in temperature and moisture. In the northern spring (April) and fall (October), for the quite symmetrical solar irradiance distribution at that time, surface downward longwave fluxes also have a symmetrical distribution with respect to the equator. In the northern summer (July) and winter (January), the maps of clear sky surface downward fluxes show a shift northward and southward respectively with the changing seasons. This result is consistent with the fact that clear sky downward fluxes are determined by the near surface temperature which is closely related to the incident solar energy. Evidently, the high values (larger than 400 Wm^{-2}) in Southeast Asia correspond to areas where, due to the high surface temperature of islands, the atmosphere is warmer than elsewhere along the same latitudinal belt. In particular, there is an area with values larger than 420 Wm^{-2} centered east of Papua New Guinea in January 1986, corresponding to very warm and moist near surface conditions. In contrast, the low values (less than 200 Wm^{-2}) near the polar regions correspond to areas where the atmosphere is cold and dry throughout the year.

Over the continents, symmetrical distributions of clear sky downward fluxes disappear and more complicated features of distributions emerge, corresponding to the land surface. There is a pronounced center of low values of downward fluxes over the Tibetan Plateau in Asia throughout the year because the mean elevation of the Tibetan Plateau is more than 4000 m above sea level so that surface air temperature is quite low except in summer. However even though high temperatures often occur there in summer, its high elevation makes the air still very dry. Since the major contribution to longwave downward flux at the surface comes from the water vapor in the lower atmosphere, the dry air over that region results in an area of low values

of downward fluxes. Over southern Africa, relatively higher values along the same latitude result from the higher air temperature and more moist air. In northern Africa, although the surface temperature is very high, the dry air, due primarily to its desert areas, results in downward fluxes that are lower along the same latitude. In addition, a pronounced trough line along the Rocky Mountains in Fig. 3 represents higher altitudes and a drier atmosphere in that region compared to surrounding areas.

Surface downward longwave fluxes, as derived from the formula described in equation (1) with given clear sky fluxes and the longwave CRF at the surface, are presented in Fig. 4 for April, July and October 1985 and January 1986 respectively. Over the oceanic areas, the zonal distribution for the clear sky case is no longer apparent. The presence of clouds increases the downward fluxes at the surface globally throughout the year. Fluxes with values larger than 400 Wm^{-2} are found over areas associated with the intense convective cloud systems, such as the ITCZ, as well as the summer and winter monsoon areas. It is reasonable because, in these regions, clouds occur frequently and the air temperatures are high. An area with values larger than 440 Wm^{-2} is found over northeast Australia in January 1986, corresponding to the high temperatures in the austral summer. Also, an area with high values is centered over southwest Indonesia in July 1985. The maps for July 1985 and January 1986 compare quite well with the corresponding results of Wu and Cheng (1989) for 1979. Their results were obtained using a physical model based on HIRS 2/MSU retrievals.

Compared with clear sky maps, larger changes occur over land than over the oceans throughout the year. In addition, the regions of high values are still distinguishable in these months except in April 1985. Low downward fluxes (less than 280 Wm^{-2}) are found over high latitudes and polar regions, where the precipitable water is low and air temperature is cold. As seen in Fig. 4, contour lines of downward fluxes are spaced very densely in high latitudes during the whole year. As we mentioned before, these sharp changes perhaps result from uncertainties in modeling the meteorological parameters in these regions, an unavoidable consequence of the inability to distinguish cloud cover from background snow and ice and hence compute the cloud forcing. In addition, seasonal variations of surface downward fluxes are still notable in Fig. 4, even though they are not as remarkable as in the clear sky case.

c. Net Upward Longwave Radiation Flux at the Surface (ocean only)

The clear sky net upward longwave flux at the surface is the difference of the upward flux minus the downward surface flux assuming no clouds. The upward flux here is computed from the sea surface temperature, which is a reported parameter in ISCCP C1 satellite data. There are three surface temperatures (TS) provided by ISCCP: mean TS from a clear sky

composite, mean TS for IR-clear pixels, and mean TS for VIS/IR-clear pixels for only day time. In order to compute the surface emission, it is not necessary to use any of these fields but instead rely on an independent source such as the sea surface temperature provided by NOAA's Climate Analysis Center (CAC). This is a blend of in situ data, advanced very high resolution radiometer (AVHRR) satellite data, and ice data (Reynolds 1988). Fig. 5 shows the zonally averaged sea surface temperatures for January 1986 for the three ISCCP fields and the CAC field. In high latitude regions, the CAC sea surface temperature is much higher than the ISCCP values because ice surface temperature is set to be the freezing point of sea water (-1.8°C). Fig. 5 indicates that the clear sky composite TS is warmest among the three ISCCP sea surface temperatures, while the IR clear sky TS is the coldest. This is to be expected since IR clear pixels are contaminated by low level clouds. We chose the VIS/IR clear sky as the most representative quantity for this study.

The difference between the surface emission computed from daytime mean TS for VIS/IR clear pixels and the CAC sea surface temperature is presented in Fig. 6 for January 1986. This difference is a measure of the uncertainty one may expect in the upward longwave radiation flux computed using different sources for the sea surface temperatures. The dominant feature of this map is a set of biases of less than 10 Wm^{-2} present over the tropical and subtropical regions except around southeast Asia, where the surface emission from mean TS for VIS/IR clear pixels exceeds that from CAC temperature by as much as 30 Wm^{-2}. This could be a result of differences in the particular algorithms used by ISCCP and CAC to account for water vapor absorption in the atmospheric window. Also any ship observations used are not necessarily representative of the skin temperature of the ocean surface. The areas with differences larger than 10 Wm^{-2} are found over high latitudes in the Pacific and Atlantic Ocean. Positive differences (less than 10 Wm^{-2}) are located over the central Pacific ocean and eastern Indian ocean, whereas areas with negative difference are found in other locations. The maximum absolute difference is only around 5%. Therefore, the agreement between the two upward fluxes is generally good for this month.

Fig. 7 shows the clear sky net upward longwave fluxes at the surface for April, July and October 1985 and January 1986 respectively. Physically the maps of clear sky net upward longwave fluxes primarily reflect the distribution of water vapor content in the boundary layer. The area with lowest values is found over Southeastern Asia throughout the year. In this region, even in the absence of clouds, the clear sky net upward longwave fluxes are quite small because of the high water vapor mixing ratio near the surface. Areas with values larger than 100 Wm^{-2} are found over the mid-latitude subsidence zones between 15° and 45° latitude in both hemispheres in April, October 1985 and January 1986, and in the southern hemisphere in July 1985. These are regions in which a dry atmosphere overlies a moderately warm ocean surface.

Also, in July 1985, there is a minimum of less than 40 Wm^{-2} off the coast of central America and, in the other three months, a minimum of less than 40 Wm^{-2} just along the west coast of Colombia, Ecuador and Peru; all these minima correspond to the presence of a relatively moist atmosphere.

Net upward longwave flux, a difference field of the clear sky net upward flux minus the surface longwave CRF (Fig. 2) as described in equation (1), is presented in Fig. 8 for April, July and October 1985 and January 1986. In this case, the areas with smaller values are still found over Southeast Asia. When it is clear, the value is low because the boundary layer is moist; when it is cloudy, there is enhanced downward emission. Also, small net upward fluxes with values less than 40 Wm^{-2} are found in high latitudes and polar regions where there is persistent cloud cover and temperatures are low throughout the year. Values larger than 80 Wm^{-2} are found over some areas in the tropical and mid-latitude zone. It is worth noting that the negative values near the Antarctic in July 1985 result from the large longwave CRF at the surface derived previously. Since negative values are possible but unlikely, one may conclude that the unreasonable high surface CRF is a result of the modeling and computation errors but not physical processes. Generally, the influence of clouds in the stratus regime causes the net longwave flux to be reduced by 50-60 Wm^{-2} throughout the year. These maps again show features similar to those obtained by Wu and Cheng (1989).

4. Discussion

Monthly mean longwave radiation fluxes at the surface for four months have been determined from currently available satellite data. Because of the diurnal variation of surface temperature over the continents, surface net longwave fluxes, which involve the surface temperatures, are presented only over the oceanic areas. The method discussed here avoids the use of an independent estimate of the frequency of occurrence of clouds or even cloud top heights in determining the surface longwave fluxes. Current methods of modeling the longwave radiation processes in the atmosphere require certain assumptions regarding the presence of clouds and their horizontal and vertical extent. Because of the complicated nature of cloud radiation and uncertainties in the observation of clouds, large errors are inevitable in this procedure. The procedure used in this study provides an alternative means of obtaining longwave radiative fluxes at the surface without the knowledge of cloud distribution. All meteorological parameters required in this method can be obtained from currently available satellite data sets. The ISCCP data and U.S. Standard Atmosphere (COESA 1976) provide the profiles of temperature, water vapor mixing ratio and ozone as well as sea surface temperatures. The distributions of the longwave CRF at the top of the atmosphere are retrieved from ERBE

data which is currently being completed for several years of measurements.

The weakest link in this procedure is the use of simulated CRF ratios that relate the CRF at the top and surface. Errors in the cloud generation scheme of the model used will affect the ratio and hence, the final product. It is also not feasible to verify these ratios observationally on a global scale, although it would be useful to verify the model result in some specific regions where simultaneous observations at the top of the atmosphere and the surface are available over an extended period of time.

The final product can be compared with field data for a few regions and periods during which extended time observations were made from ships. Note that the fields generated are area averaged monthly means and comparisons with point measurements over short periods of time do not provide any corroboration. Observations reported by Reed and Halpern (1975) off the Oregon coast covered an eight week period in July - August 1973 and included measurements taken from two sites, one 13 km from the shore and the other 120 km away. Lind and Katsaros (1987) have reported measurements taken off the California coast during the first two weeks of November 1984. Radiation budget data from GATE (Cox and Griffith, 1979) was an amalgam of direct radiation measurements and modeled fields based on soundings. The authors point out the futility of computing area and time mean quantities directly from measurements even for a dedicated field campaign over a (relatively) small portion of the oceanic area of the globe.

The daily mean net longwave radiative flux at the surface reported by Reed and Halpern (1975) varied from 71 Wm^{-2} for days when the daily mean cloud cover was 10% - 20% to between 11 - 15 Wm^{-2} for 70% - 100% cloud cover. An unweighted mean of the ten daily mean values taken at two stations over the period July 5 - August 26 is 33 Wm^{-2}. The corresponding estimate for July 1985 from Fig. 8 is around 40 Wm^{-2}. This suggests that the procedure used here is able to provide a good measure of the mean cloud fraction which is the strongest determinant of the net longwave radiation for this region. This bears out our thesis that a reliable measure of the effect of clouds is a necessary condition for obtaining global fields of the net longwave radiation at the surface.

Lind and Katsaros (1987) have reported ship based observations of the upward and downward longwave radiation taken off the California coast from October 30 - November 14 1984. The daily mean net longwave radiation from R/P FLIP ranged from 11 Wm^{-2} to 69 Wm^{-2}. Although there is no reported cloud cover, inspection of the daily mean insolation shows that the extremes correspond to days of complete cloud cover and essentially clear skies, respectively. The mean for the 15 day period at the single station was 45 Wm^{-2}. The mean for October 1985 and January 1986 from Fig. 8 is 75 Wm^{-2}. This compares favorably with the satellite and model based results of Wu and Cheng (1989) for January 1979. The discrepancy with the point measurement is significant but it is difficult to draw any conclusions based on the information

available. From Fig. 3, the clear sky downward longwave flux for this region is about 315 Wm^{-2} in October 1985 and 275 Wm^{-2} in January 1986. The data from Lind and Katsaros (1987) indicate that the minimum daily mean value over the period was 340 Wm^{-2}, presumably on the clearest day. Inspection of the temporal data shows that the absolute minimum value reached was 300 Wm^{-2} on the night of November 7-8. This indicates that the clear sky element of the procedure is acceptable. The discrepancy is in the cloud estimate and there is no reasonable means of comparing the point measurement with an area average (for a different year). This highlights the difficulties inherent in validating global fields for a quantity that is measured only occasionally.

Some generalizations can be made about the uncertainty in the global fields. Fung et al. (1984) state that a 1 g kg^{-1} uncertainty in the water vapor mixing ratio at low levels and a 100 mb error in the cloud base each translate to a 10 Wm^{-2} uncertainty in the net longwave flux over oceans. The presence of low level haze which cannot be detected from space and is not considered in the GCM is equivalent to underestimating low cloud cover, hence surface forcing. In certain regions this error could range from 5 - 10 Wm^{-2}. Moreover, if one makes the gross assumption that low clouds cover the oceans 50% of the time everywhere, it may be shown that the net longwave at the surface will range from 40 - 60 Wm^{-2} for any reasonable temperature and mixing ratio profile. The departure from this range of values shown in Fig. 8 is the true information contained in the maps and reflects the satellite based cloud information that has been used.

5. Conclusions

An attempt has been made to produce monthly mean global fields of the net longwave radiation flux at the surface over the oceans without resorting to direct measurements. The key ingredients in the technique are the satellite derived temperature and moisture profiles (which are available operationally), the top of the atmosphere cloud radiative forcing from ERBE (which is an experimental data product but could be available in the future) and the cloud distributions from a general circulation model. It should be stressed that the actual cloud cover generated by the model (which is subject to a great deal of uncertainty) is not used directly, but only information on cloud type is used through a ratio of the cloud radiative forcing at the top and surface. This parameter has the advantage that it involves simulated radiation fluxes and not the cloud fraction. The latter quantity may vary considerably from model to model and also be quite different from satellite derived estimates. However, the radiation parameterization is usually such that the fluxes at the top of the atmosphere simulated by these models compare quite favorably with observations. Examples of this apparent contradiction are in Harshvardhan et al.

(1989), and Kiehl and Ramanathan (1990).

Although it is preferable to map global fields of the longwave radiation at the surface using space and ground based measurements alone, it is evident that the introduction of large scale numerical models into this effort is unavoidable. The surface is inaccessible to space based instruments at these wavelengths under cloudy conditions. Moreover, since the fluxes are extremely sensitive to water vapor mixing ratios near the surface, even clear sky estimates are subject to a great deal of uncertainty. Any global surface measurement program over the oceans is impractical. Hybrid techniques such as the one reported here that use several sources of data, both real and simulated, are the only options.

Acknowledgements

This study has been supported by NASA Grant NAG5-1125. We wish to thank Ms. Lola Olsen and her group at NSSDC, Goddard Space Flight Center, for their promptness in supplying us with all the satellite data used in this study, Dave Randall and Donald Dazlich of CSU for providing us with the GCM results, Diane Milgate for help with the graphics, and Wanda Curtis for typing the manuscript. We also wish to acknowledge the useful suggestions provided by an anonymous reviewer.

REFERENCES

Ardanuy, P.E., L.L. Stowe, A. Gruber, M. Weiss and S.L. Craig, 1989: Longwave cloud radiative forcing as determined from Nimbus-7 observations. *J. Climate*, **2**, 766-799.

Breon, F.-M., R. Frouin and C. Gautier, 1991: Downward longwave irradiance at the ocean surface: an assessment of in situ measurements and parameterizations. *J. Appl. Meteor.*, **30**, 17-31.

Charlock, T.P., and V. Ramanathan, 1985: The albedo field and cloud radiative forcing produced by a general circulation model with internally generated cloud optics. *J. Atmos. Sci.*, **42**, 1408-1429.

Chou, M.D., 1985: Surface radiation in the tropical pacific. *J. Climate Appl. Meteor.*, **24**, 83-92.

COESA, U.S. Standard Atmosphere, 1976: U.S. Government Printing Office, Washington D. C.

Cox, S.K., and K.T. Griffith, 1979: Estimates of radiative divergence during phase III of GATE, I, Methodology. *J. Atmos. Sci.* **36**, 576-585.

Darnell, W.L., S.K. Gupta and W.F. Staylor, 1983: Downward longwave radiation at the surface from satellite measurement. *J. Climate Appl. Meteor.* **22**, 1956-1960.

Darnell, W.L., S.K. Gupta and W.F. Staylor, 1986: Downward longwave surface radiation from sun-synchronous satellite data: Validation of methodology. *J. Climate Appl. Meteor.* **25**, 1012-1021.

Frouin, R., C. Gautier and J. Morcrette, 1988: Downward longwave irradiance at the ocean surface from satellite data: Methodology and in situ validation. *J. Geophys. Res.*, **93**, 597-619.

Fung, I.Y., D.E. Harrison, and A.A. Lacis, 1984: On the variability of the net longwave radiation at the ocean surface. *Rev. of Geophys. and Space Phys.*, **22**, 177-193.

Gautier, C., G. Diak and S. Masse, 1980: A simple physical model to estimate incident solar radiation at the surface from GOES satellite data. *J. Appl. Meteor.*, **19**, 1005-1012.

Gupta, S.K., 1989: A parameterization for longwave surface radiation from sun-synchronous satellite data. *J. Climate*, **2**, 305-320.

Harrison, E.F., P. Minnis, B.R. Barkstrom, V. Ramanathan, R.D. Cess, and G.G. Gibson, 1990: Seasonal variation of cloud radiative forcing derived from the Earth radiation budget experiment. *J. Geophys. Res.*, **95**, 18,687-18,703.

Harshvardhan, D.A. Randall, T.G. Corsetti and D.A. Dazlich, 1989: Earth radiation budget and cloudiness simulations with a general circulation model. *J. Atmos. Sci.*, **46**, 1922-1942.

Harshvardhan, D.A. Randall, and D.A. Dazlich, 1990: Relationship between the longwave cloud radiative forcing at the surface and the top of the atmosphere. *J. Climate*, **3**, 1435-1443.

Justus, C.G., M.V. Paris and J.D. Tarpley, 1986: Satellite-measured insolation in the United States, Mexico, and South America. *Remote Sens. Envir.*, **20**, 57-83.

Kiehl, J.T., and V. Ramanathan, 1990: Comparison of cloud forcing derived from the Earth Radiation Budget Experiment with that simulated by the NCAR community climate model. *J. Geophys. Res.*, **95**, 11,679-11,698.

Lind, R.J., and K.B. Katsaros, 1987: Radiation measurements from R/P FLIP and R/V Acania during the Mixed Layer Dynamics Experiment (MILDEX). Technical Report, Dept. of Atmospheric Sciences, University of Washington, Seattle, WA., 44 pp. (available from the authors).

Pinker, R.T. and J.A. Ewing, 1985: Modeling surface solar radiation: Model formulation and validation. *J. Climate Appl. Meteor.*, **24**, 389-401.

Ramanathan, V., 1986: Scientific use of surface radiation budget data for climate studies. *Surface Radiation Budget for Climate Studies.* J.T. Suttles and G. Ohring, Eds., NASA reference publication 1169, 132pp.

Ramanathan, V., 1987: The role of Earth radiation budget studies in climate and general circulation research. *J. Geophys. Res.*, **92**, 4075-4095.

Randall, D.A., Harshvardhan, D.A. Dazlich and T.G. Corsetti, 1989: Interactions among radiation, convection, and large-scale dynamics in a general circulation model. *J. Atmos. Sci.*, **46**, 1943-1970.

Randall, D.A., Harshvardhan, and D.A. Dazlich, 1991: Diurnal variability of the hydrologic cycle in a general circulation model. *J. Atmos. Sci.*, **48**, 40-62.

Raschke, E., and H.J. Preuss, 1979: The determination of solar radiation budget at the Earth's surface from satellite measurements. *Meteor. Rundsch.*, **32**, 18-28.

Reed, R.K., and D. Halpern, 1975: Insolation and net longwave radiation off the Oregon coast. *J. Geophys. Res.*, **80**, 839-844.

Reynolds, R. W., 1988: A real-time global sea surface temperature analysis. *J. Climate,* **1**, 75-86.

Rossow, W.B., and R.A. Schiffer, 1991: ISCCP Cloud data products. *Bull. Amer. Meteor. Soc.*, **72**, 2-20.

Schmetz, P., J. Schmetz and E. Raschke, 1986: Estimation of daytime downward longwave radiation at the surface from satellite and grid point data. *Theor. Appl. Climatol.*, **37**, 136-149.

Tarpley, J.D., 1979: Estimating incident solar radiation at the surface from geostationary satellite data. *J. Appl. Meteor.*, **18**, 1172-1181.

WCP-92, 1984: World Climate Research Programme, WMO, GENEVA, Switzerland.

Weare, B.C., 1989: Relationships between net radiation at the surface and the top of the atmosphere derived from a general circulation model. *J. Climate,* 2, 193-197.

Wu, M.-L.C., and C.-P. Cheng, 1989: Surface downward flux computed by using geophysical parameters derived from HIRS 2/MSU soundings. *Theor. Appl. Climatol.*, **40**, 37-51.

Figure Captions

Figure 1. Flow diagram of the procedure to obtain maps of the monthly mean net upward longwave radiation flux at the surface using information provided by a general circulation model (GCM), data from the Earth Radiation Budget Experiment (ERBE) and the International Satellite Cloud Climatology Project (ISCCP).

Figure 2. Monthly mean longwave cloud radiative forcing at the surface for April, July, October 1985 and January 1986 obtained from ERBE top-of-the-atmosphere cloud forcing and GCM simulations of cloudiness.

Figure 3. Monthly mean clear sky downward longwave radiation flux at the surface for April, July, October 1985 and January 1986 obtained from TOVS profiles on the ISCCP C1 tapes and a broad band radiation code.

Figure 4. Monthly mean atmospheric downward longwave radiation flux at the surface for April, July, October 1985 and January 1986 obtained from the clear sky values shown in Figure 3 and the cloud forcing shown in Figure 2.

Figure 5. Zonal mean sea surface temperatures (SST) for January 1986 from three different parameters on the ISCCP C1 tapes and the blended SST from the Climate Analysis Center (CAC).

Figure 6. Difference between the monthly mean surface emission in Wm^{-2} for January 1986 computed using the CAC SST and the VIS/IR clear TS on the ISCCP C1 tapes. A positive difference indicates that the surface emission implied by the CAC SST is higher.

Figure 7. Monthly mean clear sky net upward longwave radiation flux at the ocean surface for April, July, October 1985 and January 1986.

Figure 8. Monthly mean atmospheric net upward longwave radiation flux at the ocean surface for April, July, October 1985 and January 1986.

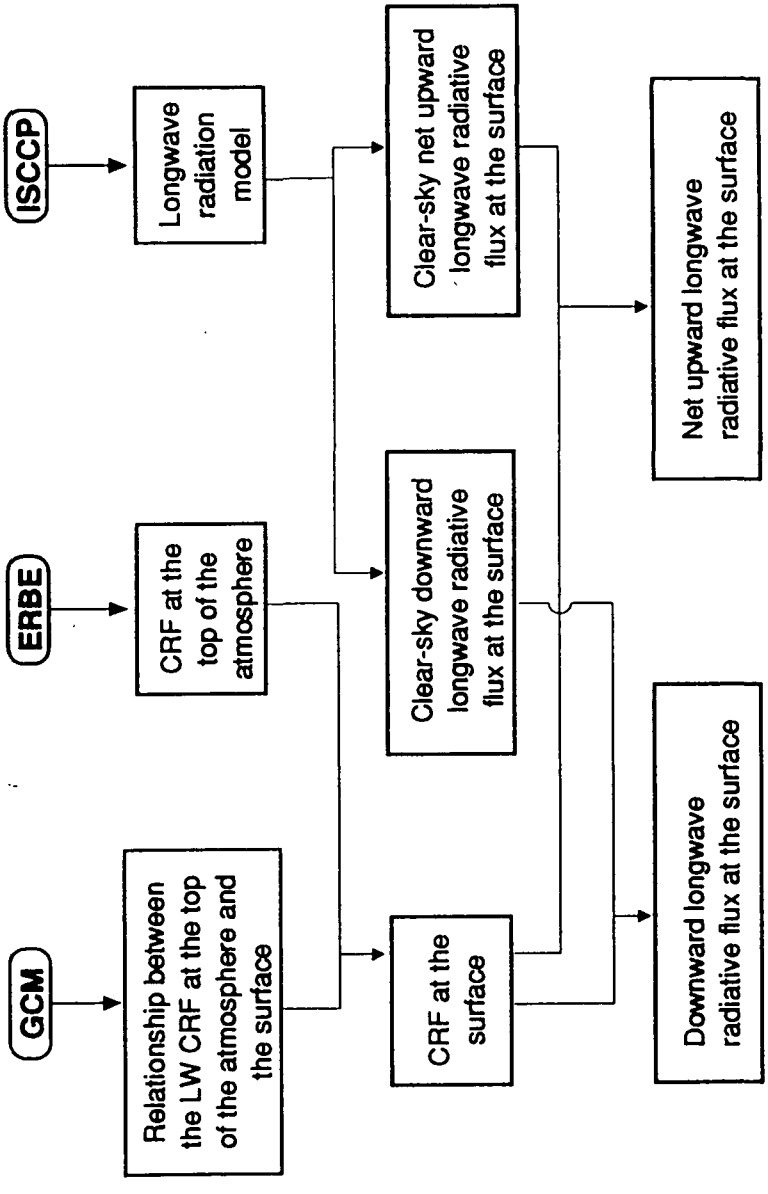
GCM
ERBE
ISCCP
Relationship between the LW CRF at the top of the atmosphere and the surface
CRF at the top of the atmosphere
Longwave radiation model
CRF at the surface
Clear-sky downward longwave radiative flux at the surface
Clear-sky net upward longwave radiative flux at the surface
Downward longwave radiative flux at the surface
Net upward longwave radiative flux at the surface

Figure 1

Longwave Cloud Radiative Forcing at the Surface

($W\ m^{-2}$)

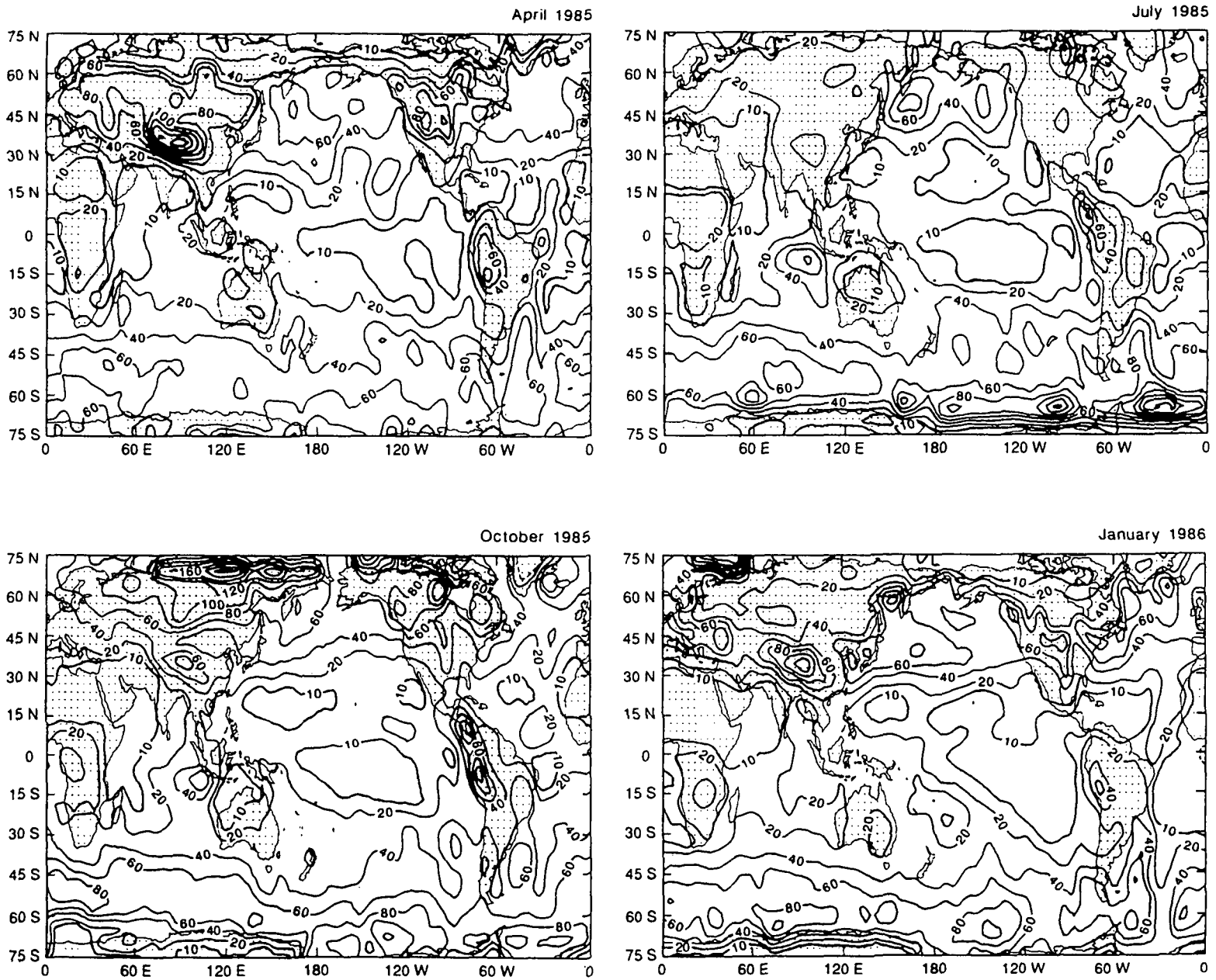

Figure 2

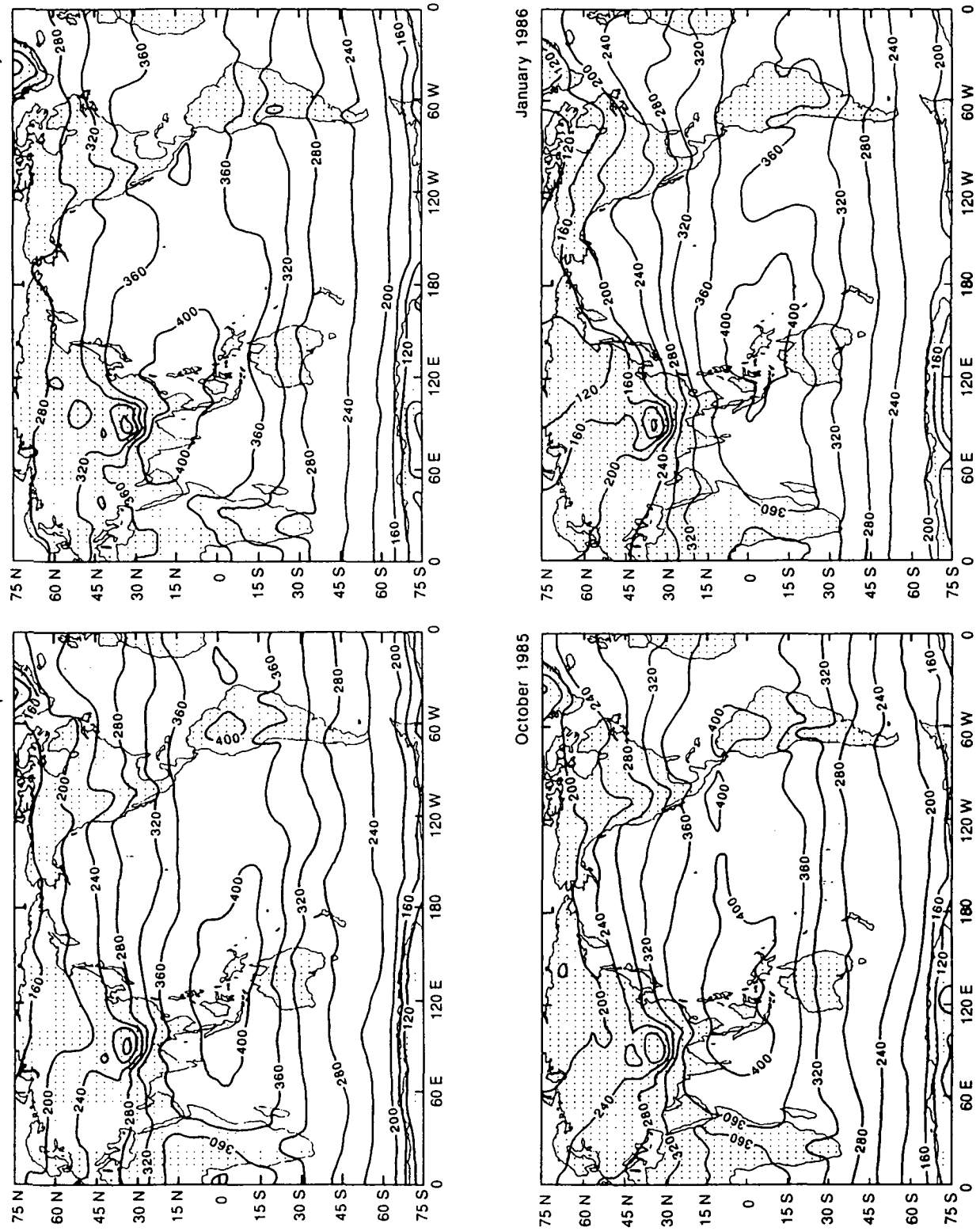
Clear Sky Downward Longwave Flux at the Surface
(W m^{-2})
July 1985
April 1985
January 1986
October 1985
75 N
60 N
45 N
30 N
15 N
0
15 S
30 S
45 S
60 S
75 S
0
60 E
120 E
180
120 W
60 W
0
160
200
240
280
320
360
400

Figure 3

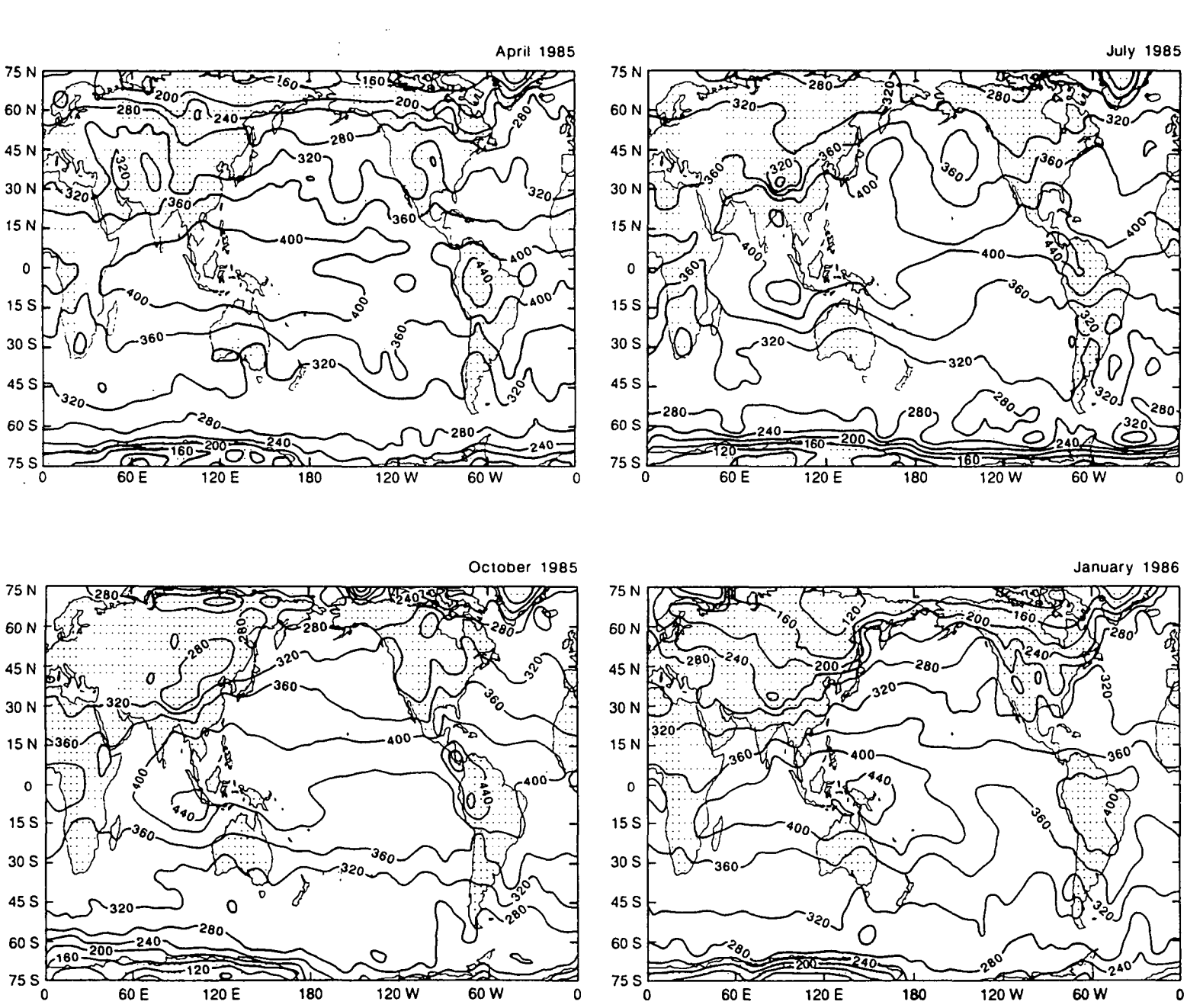
Atmospheric Downward Longwave Flux at the Surface
(W m^{-2})
April 1985
July 1985
October 1985
January 1986
75 N
60 N
45 N
30 N
15 N
0
15 S
30 S
45 S
60 S
75 S
0
60 E
120 E
180
120 W
60 W
0

Figure 4

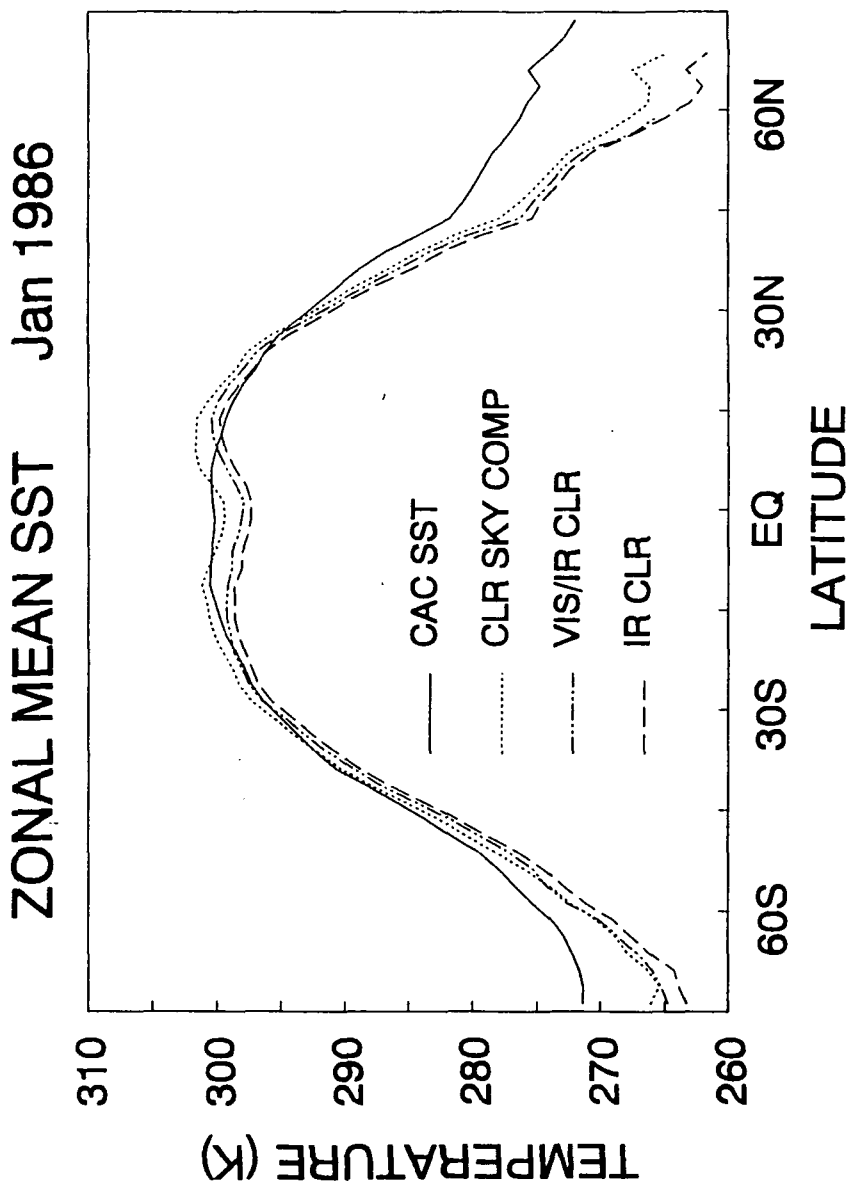
ZONAL MEAN SST Jan 1986
CAC SST
CLR SKY COMP
VIS/IR CLR
IR CLR
TEMPERATURE (K)
310
300
290
280
270
260
60S
30S
EQ
30N
60N
LATITUDE

Figure 5

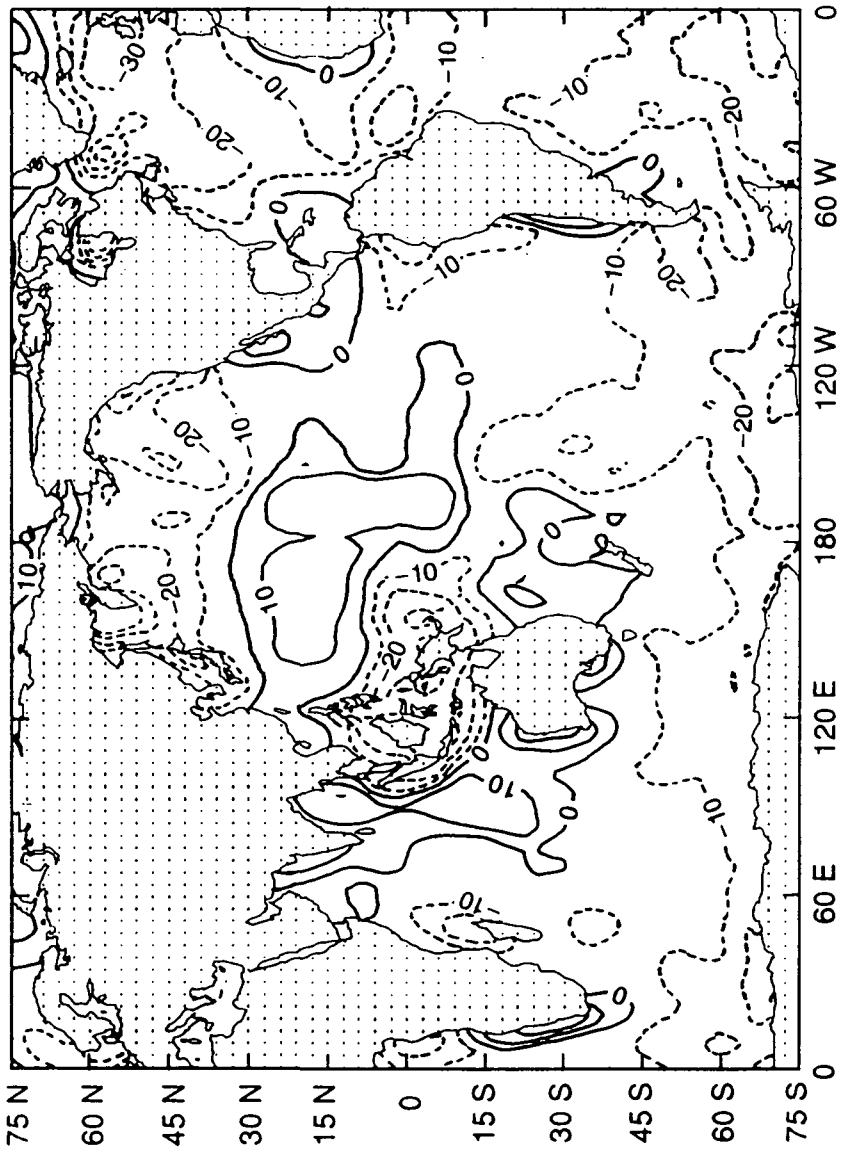
75 N
60 N
45 N
30 N
15 N
0
15 S
30 S
45 S
60 S
75 S
0
60 E
120 E
180
120 W
60 W
0

Figure 6

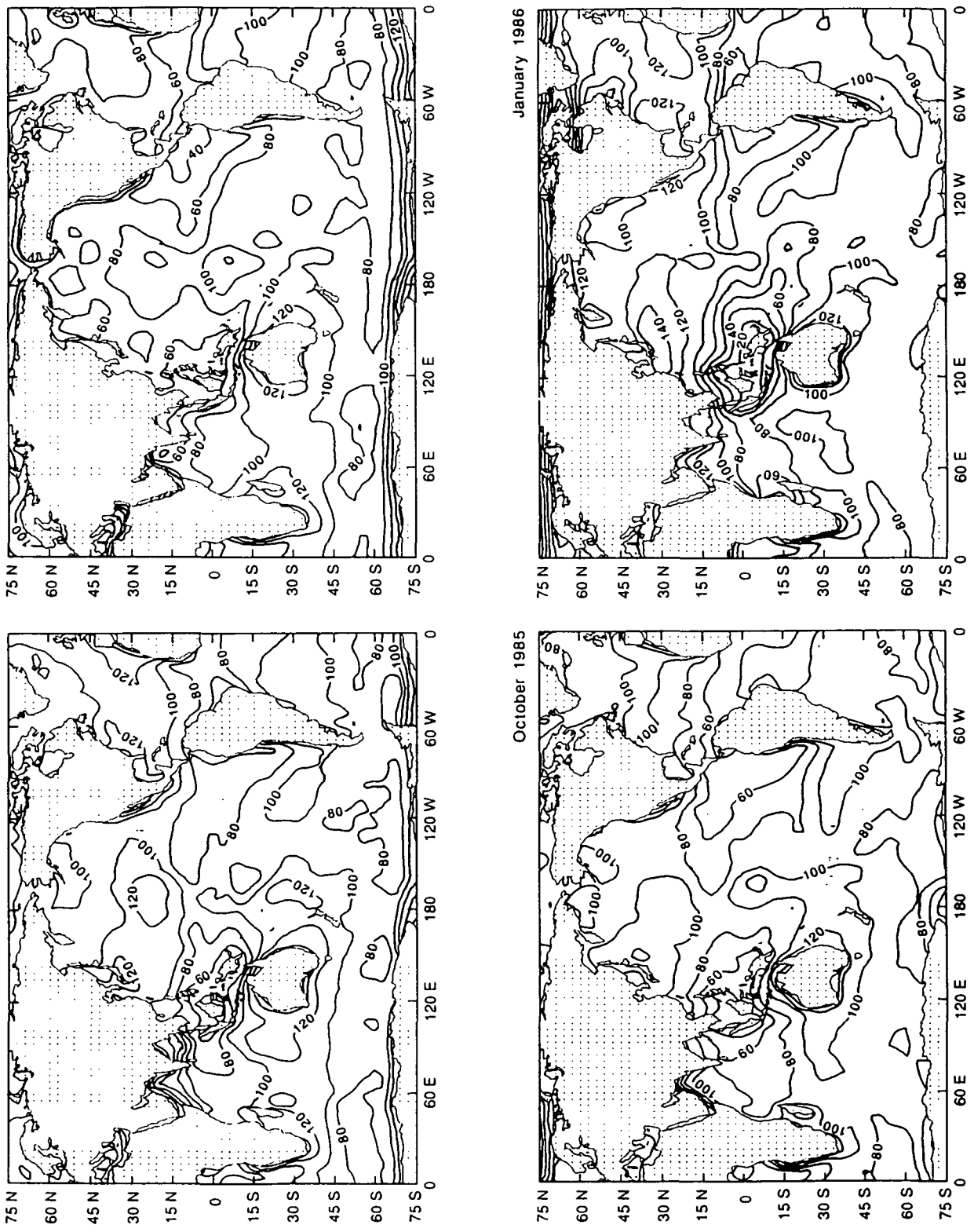
Clear Sky Net Upward Longwave Flux at the Surface
(W m^{-2})
July 1985
April 1985
January 1986
October 1985
75 N
60 N
45 N
30 N
15 N
0
15 S
30 S
45 S
60 S
75 S
0
60 E
120 E
180
120 W
60 W
0

Figure 7

Atmospheric Net Upward Longwave Flux at the Surface

($W\ m^{-2}$)

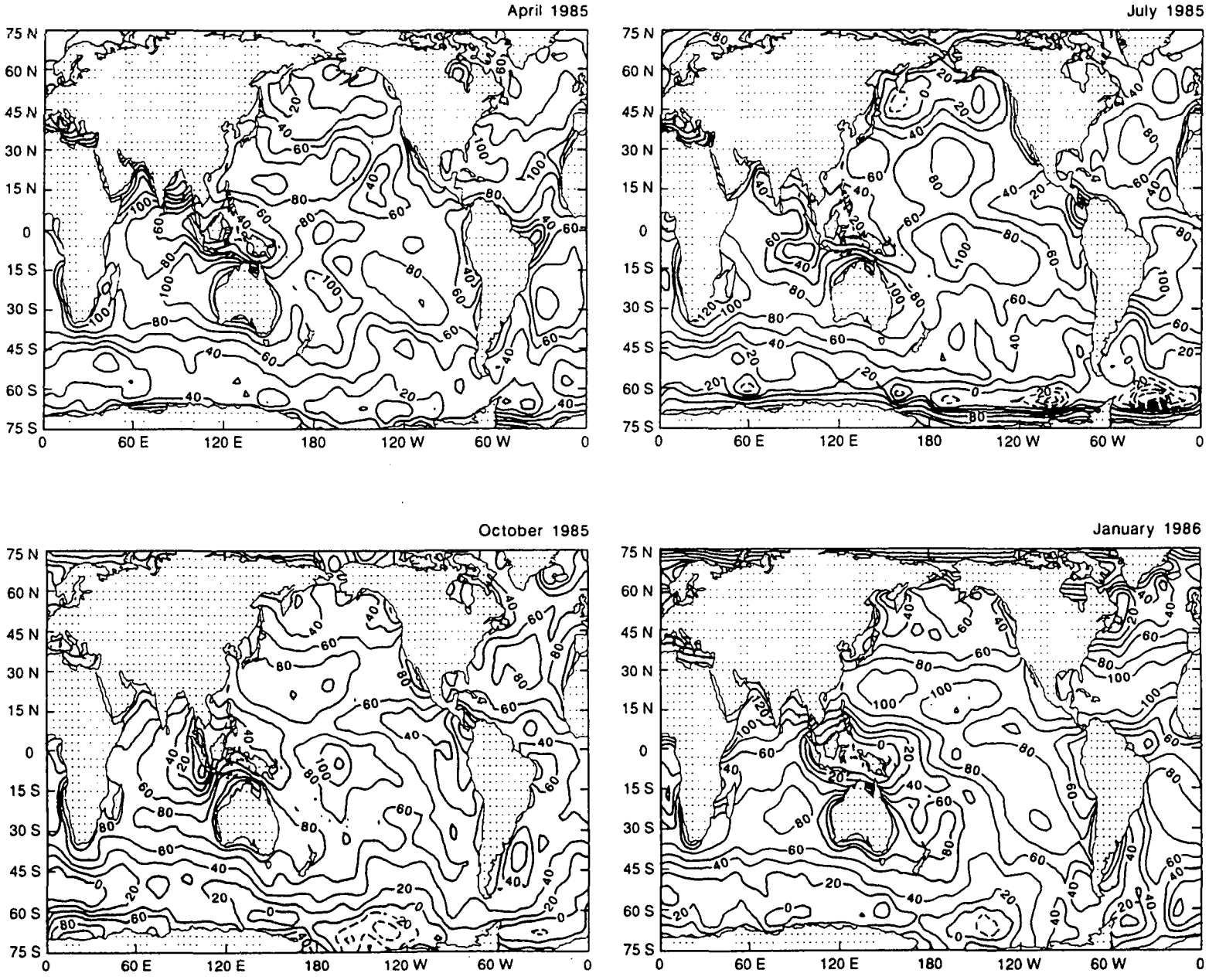

Figure 8

COMPARATIVE ACCURACY OF DIFFUSE RADIATIVE PROPERTIES COMPUTED USING SELECTED MULTIPLE SCATTERING APPROXIMATIONS

HARSHVARDHAN

Department of Earth and Atmospheric Sciences

Purdue University

West Lafayette, IN 47907

MICHAEL D. KING

Laboratory for Atmospheres, NASA/Goddard Space Flight Center

Greenbelt, MD 20771

ABSTRACT

Computational results have been obtained for the spherical albedo, global transmission, and global absorption of plane-parallel layers composed of cloud droplets. These computations, obtained using the doubling method for the entire range of single scattering albedos ($0 \leq \omega_0 \leq 1$) and for optical depths between 0.1 and 100, are compared with corresponding results obtained using selected multiple scattering approximations. Both the relative and absolute accuracies of asymptotic theory for thick layers, three diffuse two-stream approximations, and two integrated two-stream approximations are presented as a function of optical thickness and single scattering albedo for a scattering phase function representative of cloud droplets at visible wavelengths. The spherical albedo and global absorption computed using asymptotic theory are found to be accurate to better than 5% for all values of the single scattering albedo, provided the optical thickness exceeds about 2. The diffuse two-stream approximations have relative accuracies that are much worse than 5% for the spherical albedo over most of the parameter space, yet are accurate to within 5% in the global absorption when the absorption is significant. The integrated delta-Eddington scheme appears to be the most suitable model over the entire range of variables, generally producing relative errors of less than 5% in both the spherical albedo and global absorption.

1. Introduction

The role of clouds in determining the Earth's radiation budget has led to increased interest in the parameterization of the radiative properties of cloud layers in numerical atmospheric models. Recent work has been concerned with relating cloud microphysics to optical properties (Slingo 1989) which can then be used in radiative transfer schemes within models. Most models now use some form of approximation to compute cloud radiative properties, such as the plane albedo from a given set of optical properties (optical thickness, single scattering albedo, etc.) Whereas in the past these optical properties were generally fixed, there is now increasing use of interactive schemes in which cloud optical properties are generated internally by the model (Charlock and Ramanathan 1985; Harshvardhan et al. 1989).

As cloud fields evolve during a model integration, the optical properties of the generated clouds and models of gaseous absorption are used in a radiative transfer scheme to provide the shortwave and longwave radiative energy field through the atmosphere. These computations need to be carried out at each model grid point at least every time the model cloud fields are updated. In models that resolve the diurnal cycle, this could be every three hours of simulated time or even hourly. The computational burden is such that rapid yet accurate techniques are essential. In the shortwave, a common procedure is the computation of cloud layer properties by a two– stream method and the adding of radiative fluxes through the atmosphere in an energy conserving scheme (Lacis and Hansen 1974; Coakley et al. 1983; Charlock and Ramanathan 1985; Geleyn and Hollingsworth 1979; Harshvardhan et al. 1987) although the two-stream equations can also be solved directly for multiple layers using matrix solvers (Wiscombe 1977; Toon et al. 1989). The flux adding method is essentially a severely truncated form of the adding-doubling method (Hansen and Travis 1974) using upward and downward fluxes instead of intensities.

In order to compute radiative fluxes through several atmospheric layers by the flux adding method, the radiative properties of cloud layers for two different sources are required (Harshvardhan et al. 1987; Kiehl et al. 1987). When collimated solar radiation is incident on an

isolated cloud layer at some zenith angle with respect to the vertical direction, the fluxes emergent from the layer in the upward and downward directions are determined by the plane albedo and total transmission of the layer respectively. If the incident source is diffuse, the emergent flux may be obtained by an angular integration over the incident intensity field. In two–stream methods, the angular distribution of the incident intensity field is not resolved and a common practice is to assume an isotropic diffuse source. For example, in a multi– layer cloud system, the diffuse solar flux transmitted through the upper layer is the incident source for the lower layer. Also in the case of a cloud layer overlying a reflecting ground surface, multiple reflections between the cloud and ground are considered by assuming an isotropic diffuse source at the bottom boundary of the cloud layer. These diffuse radiative properties have also been used in the past to provide estimates of global effects of aerosol layers (Chýlek and Coakley 1974). A comprehensive study of the accuracy of various multiple scattering approximations for the plane albedo, total transmission and fractional absorption of isolated cloud layers corresponding to incident collimated radiation was presented by King and Harshvardhan (1986a, b). The present study complements the earlier one in assessing the accuracy of various approximations for calculating the radiative properties of cloud and aerosol layers for an incident isotropic diffuse source.

The presentation follows the organization of King and Harshvardhan (1986a; hereafter referred to as KH). Section 2 discusses multiple scattering calculations used to obtain the diffuse radiative properties of cloud layers of varying optical thicknesses and single scattering albedos. These computational results, obtained with the doubling method, will be considered the benchmark solutions with which various multiple scattering approximations will be compared. Section 3 introduces the asymptotic theory approximation and the general class of two-stream approximations that we will consider. Section 4 presents the results of the comparison between the approximate and exact results in terms of absolute and relative differences. A discussion of the results follows in Section 5. Section 6 is a summary including recommendations for using these approximations.

2. Multiple scattering computations

To assess the accuracy of various multiple scattering approximations, radiative transfer computations were performed using the doubling method described by Hansen and Travis (1974), together with the invariant imbedding initialization described by King (1983). These computations were performed for a cloud drop size distribution typical of fair weather cumulus (FWC) clouds (Hansen 1971), and were performed at a wavelength $\lambda = 0.754\mu m$ assuming a refractive index of liquid water m = 1.332. A detailed description of the cloud model, together with an illustration of the single scattering phase function, can be found in KH. The azimuth-independent terms of the reflection and transmission functions were used to obtain the plane albedo $r(\tau_t,\mu_0)$ and total transmission $t(\tau_t,\mu_0)$ as a function of τ_t, the total optical thickness of the layer, and μ_0, the cosine of the solar zenith angle. In terms of these functions the spherical albedo, global transmission and global absorption of the layer are given by

$$\bar{r}(\tau_t) = 2\int_0^1 r(\tau_t,\mu_0)\mu_0 d\mu_0, \tag{1}$$

$$\bar{t}(\tau_t) = 2\int_0^1 t(\tau_t,\mu_0)\mu_0 d\mu_0, \tag{2}$$

$$\bar{a}(\tau) = 1 - \bar{r}(\tau_t) - \bar{t}(\tau_t). \tag{3}$$

In order to cover a wide range of applications, these computations were performed for values of the single scattering albedo ranging from pure absorption ($\omega_0 = 0$) to conservative scattering ($\omega_0 = 1$). The single scattering phase function was left unchanged such that all computations apply to a phase function having an asymmetry factor g = 0.843.

Figure 1 illustrates numerical computations of the spherical albedo $[\bar{r}(\tau_t)]$, global transmission $[\bar{t}(\tau_t)]$ and global absorption $[\bar{a}(\tau_t)]$ as a function of ω_0 and τ_t. The doubling

computations used to generate these results were obtained at twelve optical depths 0.0625, 0.125, ..., 128 interleaved with another set of eleven optical depths 0.0884, 0.1768, ..., 90.51. Each set of doubling computations was itself made at each of 31 values of the single scattering albedo. The single scattering albedo scale is linear in the similarity parameter s, defined by

$$s = \left[\frac{1 - \omega_0}{1 - \omega_0 g}\right]^{1/2}. \qquad (4)$$

This makes it possible to expand the scale in the vicinity of conservative scattering ($\omega_0 = 1$) and still to span the full range $0 \leq \omega_0 \leq 1$. The angular computations, including the integration in (1) and (2), were performed at 80 Gaussian quadrature points. As in KH, the computed results were first interpolated to generate a 300 × 300 matrix prior to plotting. The interpolated arrays represent the exact results to which the radiative transfer approximations are compared in Section 4.

It is perhaps pertinent to point out certain features of the radiative properties illustrated in Figure 1. For conservative or very weakly absorbing layers, the spherical albedo increases rapidly with increasing optical thickness for small values of τ_t and then much more slowly as τ_t becomes large. This is the well known non– linear behavior that leads to problems in estimating area– averaged albedos for a non– homogeneous cloud layer (Harshvardhan and Randall 1985). For moderate to strong absorption, the saturation of both the spherical albedo and global absorption at optical thicknesses of about 10 or even less is the most striking feature of Figure 1. In the near infrared, this implies that cloud absorption is primarily a function of the single scattering albedo and not the optical thickness once the cloud layer is several hundred meters thick (Twomey 1976). The importance of determining the spectral dependence of ω_0 for cloud layers and the development of accurate parameterizations for inclusion in radiative transfer models follows from this observation (King et al. 1990; Fouquart et al. 1991).

3. Radiative transfer approximations

Three classes of approximations will be considered here for comparison with the multiple scattering results presented above. In all cases, analytic or easily integrable functions relate the radiative properties to the optical properties. The three approximations we will consider are asymptotic theory for thick layers, diffuse two-stream approximations, and integrated two-stream approximations. Although there are several variations of two-stream approximations, only a few common and representative models will be considered.

a. Asymptotic theory

Asymptotic theory is a rigorous solution to the equation of transfer in optically thick layers, and as such, makes no assumption about the angular distribution of scattered radiation within the medium. Expressions for the plane albedo and total transmission of an optically thick layer under collimated illumination conditions can be found in KH and will not be repeated here. From these expressions it can be shown that the asymptotic theory approximations for the spherical albedo $[\hat{\bar{r}}(\tau_t)]$, global transmission $[\hat{\bar{t}}(\tau_t)]$ and global absorption $[\hat{\bar{a}}(\tau_t)]$ are given by

$$\hat{\bar{r}}(\tau_t) = \bar{r}_\infty - \frac{mn^2 l e^{-2k\tau_t}}{1 - l^2 e^{-2k\tau_t}}, \tag{5}$$

$$\hat{\bar{t}}(\tau_t) = \frac{mn^2 e^{-k\tau_t}}{1 - l^2 e^{-2k\tau_t}}, \tag{6}$$

$$\hat{\bar{a}}(\tau_t) = 1 - \hat{\bar{r}}(\tau_t) - \hat{\bar{t}}(\tau_t), \tag{7}$$

for nonconservative scattering ($\omega_0 < 1$). In these expressions $\bar{r}_\infty$ is the spherical albedo of a semi-infinite atmosphere and m, n, l and k are constants (coefficients) that depend primarily on the similarity parameter given by (4). All of the functions and constants that appear in these expressions can be computed by equating asymptotic formulae and doubling results at three values of the optical thickness for which asymptotic theory is valid (viz., $\tau_t = 8$, 16 and 32), as

first pointed out by van de Hulst (1968). Similarity relations for calculating $\bar{r}_\infty$ (denoted A* by van de Hulst 1968), m, n, l and k as a function of s for the full range $0 \le s \le 1$ can be found in Table 1 of King et al. (1990). Once these coefficients have been computed, expressions for all of the radiative properties are analytic functions that can be computed rapidly within a radiative transfer code.

For the special case of conservative scattering ($\omega_0 = 1$), Eqs. (5) and (6) reduce to

$$\hat{\bar{r}}(\tau_t) = 1 - \frac{4}{3(1 - g)(\tau_t + 2q_0)}, \tag{8}$$

$$\hat{\bar{t}}(\tau_t) = \frac{4}{3(1 - g)(\tau_t + 2q_0)} \tag{9}$$

where q_0 is the extrapolation length. The reduced extrapolation length $q' = (1\text{-}g)q_0$ is known to range between 0.709 and 0.715 for all possible phase functions (van de Hulst 1980), and has the value $q' = 0.715$ for the phase function used here. Again, one is left with simple analytic functions describing the variation of $\hat{\bar{r}}(\tau_t)$ and $\hat{\bar{t}}(\tau_t)$ as a function of τ_t for a given asymmetry factor g. The set of equations (5) – (9) form the approximations for the diffuse radiative properties of a medium based on asymptotic theory.

b. Diffuse two-stream approximations

In the absence of any direct collimated beam, the two-stream equations of radiative transfer result in a set of differential equations for the upward and downward diffuse fluxes $F^{\pm}(\tau)$ (Coakley and Chýlek 1975; Meador and Weaver 1980):

$$\frac{dF^-(\tau)}{d\tau} = \gamma_1 F^-(\tau) - \gamma_2 F^+(\tau), \tag{10}$$

$$\frac{dF^+(\tau)}{d\tau} = \gamma_2 F^-(\tau) - \gamma_1 F^+(\tau), \tag{11}$$

where $F^-(\tau)$ represents the upward flux and $F^+(\tau)$ the downward flux at optical depth τ. The equations can easily be solved subject to the boundary conditions

$$F^+(0) = F_0, \tag{12}$$

$$F^-(\tau_t) = 0, \tag{13}$$

for a diffuse isotropic source incident at the top boundary of the layer (or cloud) and for which no illumination is incident from below. The spherical albedo is thus obtained from the expression

$$\hat{r}(\tau_t) = F^-(0)/F_0 \tag{14}$$

and the global transmission from

$$\hat{t}(\tau_t) = F^+(\tau_t)/F_0. \tag{15}$$

For nonconservative scattering ($\omega_0 < 1$), the solution may be obtained in the form (Coakley and Chýlek 1975; Meador and Weaver 1980)

$$\hat{r}(\tau_t) = \frac{\gamma_2(1 - e^{-2k\tau_t})}{k + \gamma_1 + (k - \gamma_1)\, e^{-2k\tau_t}} \tag{16}$$

$$\hat{t}(\tau_t) = \frac{2k\, e^{-k\tau_t}}{k + \gamma_1 + (k - \gamma_1)\, e^{-2k\tau_t}}, \tag{17}$$

and for conservative scattering ($\omega_0 = 1$):

$$\hat{r}(\tau_t) = \frac{\gamma_1 \tau_t}{1 + \gamma_1 \tau_t}, \tag{18}$$

$$\hat{\bar{t}}\,(\tau_t) = 1 - \hat{\bar{r}}\,(\tau_t)\,. \tag{19}$$

In (16) - (19), the coefficients γ_1 and γ_2 depend on the particular two-stream approximation, with the diffusion exponent k defined as

$$k = (\gamma_1^{\,2} - \gamma_2^{\,2})^{1/2}. \tag{20}$$

Table 1 lists three diffuse two-stream models used for this study and the corresponding values of γ_1 and γ_2. The discrete ordinates model is identified as the quadrature scheme by Meador and Weaver (1980) and Toon et al. (1989). The hemispheric mean model defined by Toon et al. (1989) is similar to the Coakley-Chýlek model II referred to by KH and first introduced by Chýlek and Coakley (1974). The two stream model used by Sagan and Pollack (1967) has coefficients similar to those of both of the above mentioned models. Instead of the asymmetry parameter g, some two stream models use the average backscatter fraction $\bar{\beta}$, which is defined in KH and readily computed from the backscatter fraction $\beta(\mu_0)$, introduced by Coakley and Chýlek (1975) and Zdunkowski et al. (1980) to compute the radiative properties of layers for collimated incident sources. The Eddington model has, of course, been used widely (Shettle and Weinman, 1970). The set of equations (16) – (20) are used to compute the diffuse radiative properties for the two-stream approximations. It should be noted that these expressions have fairly simple analytic forms that favor rapid computation.

c. Integrated two-stream approximations

Extensive discussion of two-stream approximations for a collimated source can be found in KH as well as in earlier work, in particular the comprehensive treatment by Meador and Weaver (1980). Expressions for the approximate plane albedo $[\hat{r}(\tau_t, \mu_0)]$, total transmission $[\hat{t}(\tau_t, \mu_0)]$ and fractional absorption $[\hat{a}(\tau_t,\mu_0)]$ are the set of Eqs. (21) – (29) in KH. These expressions include the transformations that are required in the case of delta-scaling (Joseph et

al. 1976). To obtain comparable expressions for the diffuse radiative properties, $\hat{r}(\tau_t,\mu_0)$ and $\hat{t}(\tau_t, \mu_0)$ must be integrated according to Eqs. (1) and (2). However, these expressions are quite complicated and thus integration in a closed form is not generally practical.

An analytic expression for the spherical albedo in the Eddington and delta-Eddington approximations has been obtained by Wiscombe and Warren (1980) and involves exponential integrals that are not conducive to rapid computation within a model. For this study, $\hat{r}(\tau_t,\mu_0)$ and $\hat{t}(\tau_t,\mu_0)$ obtained by the delta-Eddington approximation were numerically integrated to provide $\bar{\hat{r}}(\tau_t)$ and $\bar{\hat{t}}(\tau_t)$. KH found that the delta-Eddington approximation for collimated illumination conditions is quite accurate over a wide range of τ_t and μ_0, especially when ω_0 is near unity. A model that performs well for optically thin layers over the limited range of ω_0 studied by KH is the plane albedo scheme of Coakley and Chýlek (1975), designated Coakley-Chýlek model I by KH. Two-stream methods for collimated sources require a third coefficient, γ_3, which appears with the source term and is thus not included in Eqs. (10) and (11). The expressions for γ_3 used by the two integrated models presented here are given in Table 1.

The integrations in Eqs. (1) and (2) required to obtain the diffuse properties are performed using 80 point Gaussian quadrature and the results should be considered identical to an analytic solution for all practical purposes. The general form of the quadrature summation is

$$\bar{r}(\tau_t) = 2 \sum_{i=1}^{N} r(\tau_t,\mu_i)\mu_i w_i \qquad (21)$$

where μ_i are the Gaussian quadrature points on the half space and w_i are the corresponding Gaussian weights. However, this detailed integration is of no practical value because the computational burden is onerous when applied to a global climate model. We have therefore also included results for the delta-Eddington and Coakley-Chýlek (I) models integrated using two-point and four-point quadrature, respectively. The diffuse radiative properties can then be obtained with a computational effort comparable to that required to compute properties for

collimated radiation.

4. Results

We have examined both the absolute and relative accuracies of the spherical albedo, global transmission and global absorption as a function of τ_t and ω_0 for the asymptotic approximation as well as the Eddington, discrete ordinates and hemispheric mean diffuse two-stream approximations. Other diffuse two-stream approximations that we have examined generally yield somewhat poorer results when compared to our doubling benchmark calculations. In addition, we have considered the integrated delta-Eddington and Coakley-Chýlek (I) approximations computed using both 80 points and a limited number of Gaussian quadrature points for integration over the solar zenith angle.

Figure 2 illustrates a 4 × 3 plot composite of results for the absolute difference in the spherical albedo, global transmission and global absorption for four of these models, where the first row applies to asymptotic theory and succeeding rows to the Eddington, discrete ordinates and hemispheric mean approximations. Individual plots in the first column of Fig. 1 represent absolute errors in the spherical albedo, defined as

$$\Delta\bar{r}(\tau_t, \omega_0) = \hat{\bar{r}}(\tau_t, \omega_0) - \bar{r}(\tau_t, \omega_0), \tag{22}$$

with succeeding columns representing corresponding errors in global transmission $[\Delta\bar{t}(\tau_t, \omega_0)]$ and global absorption $[\Delta\bar{a}(\tau_t, \omega_0)]$. With these definitions, positive (negative) errors indicate that the radiative transfer approximation overestimates (underestimates) the exact solution, taken as the computational results presented in Fig. 1. The relative errors in the spherical albedo, global transmission and global absorption are presented in Fig. 3, and are given in percent. It is necessary to consider the performance of a particular model in both a relative and an absolute sense in order to delineate a range of acceptability.

Individual contour plots in Figs. 2 and 3 have been shaded to draw attention to those regions of greatest accuracy. For example, asymptotic theory is seen to be accurate to within 5%

in reflection and absorption for $\tau_t \gtrsim 2$ and for all values of ω_0. In transmission, relative errors exceed 5% for $\omega_0 < 0.90$ and $2 \leq \tau_t < 8$ but the absolute errors are so small (<0.03) that the approximation could probably still be used without serious adverse results. It is evident from Figs. 2 and 3 that the asymptotic approximation provides accurate results for all three diffuse radiative properties over the entire range of ω_0 as long as $\tau_t \gtrsim 2$.

The three diffuse two-stream models considered here are seen to yield unacceptable errors in one or more of the radiative properties over regions that would normally be encountered in modeling applications. Although the range of acceptability will depend on the particular application, one can consider a 5% error in the spherical albedo as a standard for comparison. The spherical albedo is usually the parameter of choice in estimating the sensitivity of any radiative perturbation. However, when the value itself is small, an absolute error criterion is more useful. For optically thin layers, the absolute errors in spherical albedo are generally less than 0.01 for the discrete ordinates and hemispheric mean approximations. Errors in global transmission are similar for all three models while the Eddington and hemispheric mean models are successful in estimating the global absorption of a layer when $\omega_0 \gtrsim 0.99$ and $\tau_t \lesssim 10$ with errors of less than 1%. If the range of acceptability is relaxed to 5%, then the Eddington and hemispheric mean models can be used for absorption when ω_0 is as low as 0.95 except for optically thick layers. This covers the range of single scattering albedo encountered in water clouds throughout the visible and near-infrared spectrum (King et al. 1990).

The two integrated two-stream methods studied in this investigaton provide more accurate results for all three diffuse radiative properties as shown in Figs. 4 and 5. The delta-Eddington model was shown by KH to be highly successful in estimating the plane albedo for conservative scattering. There was a marked degradation of performance when nonconservative cases were considered. The present study shows that this model, when integrated over an isotropic diffuse incident source, provides excellent results for the spherical albedo and global transmission over most of the range of τ_t and ω_0. Errors in excess of 10% in global absorption are present for moderate optical depths ($0.5 \lesssim \tau_t \lesssim 5$) when ω_0 exceeds about 0.95. However, it

may be seen from Fig. 4 that the absolute errors in global absorption are less than 0.02 throughout this region. In addition, the large relative error in global transmission for optically thick absorbing layers is irrelevant since the global transmission is itself close to zero as is the absolute error. The Coakley-Chýlek (I) model provides results of comparable accuracy for optically thin layers. This is not surprising since KH showed that it was the most accurate of the two-stream models for this case. However, the delta-Eddington model when integrated over all incident angles is nearly as accurate as the Coakley-Chýlek (I) model for optically thin layers. Moreover, the accuracy of the integrated delta-Eddington model does not degrade as rapidly at higher optical depths.

As mentioned previously these two models would only be of academic interest if a rigorous numerical integration was required for every computation of the diffuse radiative properties. We have therefore also presented results obtained using a limited number of quadrature points in the integration over solar zenith angle [cf. Eq. (21)]. As can be seen from the second panel of Figs. 4 and 5, a two-point integration of the delta-Eddington models yields accuracies that are comparable to the accuracy obtained using an 80 point integration. However, for the Coakley-Chýlek (I) model it is necessary to use a four point integration to obtain results that are of comparable accuracy.

5. Discussion

Although the results presented here are not exhaustive in the sense that all possible approximations have not been tested, we feel they are representative of what one might expect for any class of model. All the schemes are computationally efficient and it is not necessary to perform a rigorous integration for the models based on incident collimated sources. The approximations presented here can be incorporated into a multi-layer radiative transfer module that may be added to the radiation code in a numerical model.

All computations presented here were obtained for a FWC drop size distribution having an asymmetry factor $g = 0.843$. Variations along the ω_0 axis can therefore be viewed as representing the effect of altering the gaseous absorption in the layer at a particular wavelength

or to some extent variations in the wavelength if g does not vary too greatly. This would cover the solar near-infrared spectrum over which $(1 - \omega_0)$ varies by several orders of magnitude while g generally lies between 0.80 and 0.90 (cf. King et al. 1990).

As found by KH for collimated radiative properties, the asymptotic approximation yields consistently excellent results for optically thick layers, regardless of single scattering albedo and solar zenith angle. Figures 2 and 3 show that the same is true for the diffuse radiative properties as long as $\tau_t \gtrsim 2$. In a numerical model with internally generated cloud optical properties, this requirement will not always be met. Errors become unacceptably large when $\tau_t < 1$. For this reason, the asymptotic approximation should only be used when it is known a priori that $\tau_t \geq 2$ at all times. This is the one serious shortcoming of an otherwise simple and accurate model. The method also requires a pre-computed table of coefficients m, n, k, l and $\bar{r}_\infty$ or analytic forms that compute these quantities within the program. Analytic expressions for these coefficients in terms of the similarity parameter can be found in King et al. (1990), which further discusses a remote sensing application of asymptotic theory.

The three diffuse two-stream models presented here are the simplest to implement in a numerical atmospheric model and are the most computationally efficient, but their accuracy is limited to certain regions of the parameter space. They are also not uniformly accurate for all three radiative properties. This is especially true in the Eddington approximation, where the spherical albedo is frequently too inaccurate to be of any value in a numerical model. In addition, the Eddington model yields unphysical values of the spherical albedo and global absorption when absorption is very large (King and Harshvardhan 1986b). This situation arises occasionally in the water vapor bands of the near-infrared and frequently in the thermal infrared. The problem can be rectified in a computer code with the addition of a check for unphysical values which could then be forced to the condition of zero reflection. The discrete ordinates model does not suffer from this limitation and generally yields better results for the spherical albedo than does the Eddington approximation. The somewhat poorer results for global absorption are not too important since the absolute errors are small in this case. The hemispheric

mean model yields results very similar to the discrete ordinates model except for global absorption. The smaller relative errors for weak absorption is an especially attractive feature of the hemispheric mean model which otherwise suffers from the fact that it tends to overestimate the spherical albedo by more than 5% for the very important case of nearly conservative optically thick layers.

The integrated delta-Eddington model yields excellent results for all three radiative properties over the entire range of optical properties that are encountered in the radiation code of a numerical atmospheric model. In fact, errors in the diffuse radiative properties are generally smaller than the errors found by KH for collimated radiative properties, with no unphysical results anywhere in the parameter space. There has obviously been some cancellation of errors in the angular integration. As mentioned earlier, the one error-prone region is moderate optical thickness and weak absorption. This was also true for the errors in fractional absorption for a collimated source. Since the direct beam is usually handled by a delta-Eddington or similar approximation, the coefficients and functions used for this model are usually already present in a numerical model. There is however an extra computational overhead in the angular integration in that planar properties need to be computed at several angles and then numerically integrated. However, as seen in Figs. 4 and 5, these computations need be carried out at only two points to yield results comparable to a detailed numerical integration.

The integrated Coakley-Chýlek (I) model is of limited value, except perhaps for optically thin weakly absorbing layers. There is also an added computational burden since at least four angular computations are required for the phase function used here. For collimated radiative properties and for optically thin layers, KH found that this model was superior to the delta-Eddington model. For diffuse radiative properties, on the other hand, we find that there is little advantage in using the Coakley-Chýlek (I) model, even for optically thin layers.

6. Summary and Recommendations

In the present study the spherical albedo, global transmission and global absorption computed by various radiative transfer approximations have been compared with doubling computations as a function of optical thickness and single scattering albedo. Since the entire range of ω_0 has been considered for optical depths from 0.1 to 100, the results presented here can be utilized to decide which approximate method is the most accurate for a particular application. The results presented here should be considered in parallel with the findings of KH regarding the plane albedo, total transmission and fractional absorption for a collimated incident source.

In order to summarize the results of this study, it is useful to present composite figures extracted from the individual figures to highlight regions of highest accuracy. Following van de Hulst (1980), we show in Fig. 6 the regions for which a particular model is accurate to within 1% and 5%. Only those models that are reasonably accurate in the particular radiative property have been included. These models include asymptotic theory, the two-point delta-Eddington method and the four-point Coakley-Chýlek (I) method. Although the hemispheric mean model yields acceptable results for the global absorption, it is not included here because results for the spherical albedo are generally poor.

At the 1% (5%) level, asymptotic theory can be used for all ω_0 as long as $\tau_t \gtrsim 3.5$ (2). For smaller optical depths, there is a choice that can be made between the delta-Eddington and Coakley-Chýlek(I) models, but our recommendation is to use the delta-Eddington method. Many general circulation models are already using this method to compute collimated radiative properties and the additional overhead incurred in the two-point integration should be minimal. If a scheme is needed to span the entire domain, the asymptotic method should not be used since its performance deteriorates very rapidly for $\tau_t \lesssim 3$. For this situation, typical of GCM applications, the integrated delta-Eddington scheme should yield acceptable results.

The overall errors for a multi-layer cloud system over a reflecting surface will depend on the optical thickness and single scattering albedo of the individual layers. At present it is felt

that errors in parameterizing the band averaged single scattering albedo of cloud layers in the near-infrared will dominate errors in approximating the radiative properties of individual layers (Fouquart et al. 1991). For example, the use of a single value of ω_0 to represent the entire solar near infra-red can result in errors in the layer absorption of several hundred percent (Slingo 1989). The sensitivity of all radiative properties to ω_0 can be appreciated by inspection of Figure 1. Since any scheme has to limit the number of bands for computational efficiency, the selection of these bands and the average absorbing properties used could determine the overall accuracy. However, for a given set of τ_t and ω_0 the results presented in this study could act as a guide for choosing an appropriate model. Finally, it is pertinent to mention that these accuracies refer to an idealized plane parallel model. There is, of course, the additional problem of representing inhomogeneous cloud systems including geometric effects (Harshvardhan and Thomas 1984; Stephens 1988), a problem not considered in this study.

Acknowledgments. The authors are grateful to Howard G. Meyer for aid in performing the computations, Tim Gilbert for the graphics and Wanda Curtis for typing the manuscript. This study was supported by NSF Grant ATM-8909870, NASA Grant NAG 5-1125 and the NASA Radiation Processes Research Program.

REFERENCES

Charlock, T. P., and V. Ramanathan, 1985: The albedo field and cloud radiative forcing produced by a general circulation model with internally generated cloud optics. *J. Atmos. Sci.*, **42**, 1408-1429.

Chýlek, P., and J. A. Coakley, Jr., 1974: Aerosols and climate. *Science*, **183**, 75-77.

Coakley, J. A., Jr., and P. Chýlek, 1975: The two– stream approximation in radiative transfer: Including the angle of the incident radiation. *J. Atmos. Sci.*, **32**, 409-418.

_____, R. D. Cess, and F. B. Yurevich 1983: The effect of tropospheric aerosols on the Earth's radiation budget: a parameterization for climate models. *J. Atmos. Sci.*, **40**, 116-138.

Fouquart, Y., B. Bonnel, and V. Ramaswamy, 1991: Intercomparing shortwave radiation codes for climate studies. *J. Geophys. Res.*, **96**, 8955-8968.

Geleyn, J. F., and A. Hollingsworth, 1979: An economical analytical method for the computation of the interaction between scattering and line absorption of radiation. *Contrib. Atmos. Phys.*, **52**, 1-16.

Hansen, J. E., 1971: Multiple scattering of polarized light in planetary atmospheres. Part I. The doubling method. *J. Atmos. Sci.*, **36**, 508-518.

_____, and L.D. Travis, 1974: Light scattering in planetary atmospheres, *Space Sci. Rev.*, **93**, 527-610.

Harshvardhan, and R.W.L. Thomas, 1984: Solar reflection from interacting and shadowing cloud elements. *J. Geophys. Res.*, **89**, 7179-7185.

_____, and D. A. Randall, 1985: Comments on "The parmeterization of radiation for numerical weather prediction and climate models". *Mon. Wea. Rev.*, **113**, 1832-1833.

_____, R. Davies, D. A. Randall, and T. G. Corsetti, 1987: A fast radiation parameterization for general circulation models. *J. Geophys. Res.*, **92**, 1009-1016.

_____, D. A. Randall, T. G. Corsetti, and D. A. Dazlich, 1989: Earth radiation budget and cloudiness simulations with a general circulation model. *J. Atmos. Sci.*, **46**, 1922-1942.

Joseph, J.H., W.J. Wiscombe and J.A. Weinman, 1976: The delta-Eddington approximation for radiative flux transfer. *J. Atmos. Sci.*, **33**, 2452-2459.

Kiehl, J.T., R.J. Wolski, B.P. Briegleb, and V. Ramanathan, 1987: Documentation of radiation and cloud routines in the NCAR Community Climate Model (CCM1). NCAR Technical Note NCAR/TN-288 + IA, Boulder, CO, 109 pp.

King, M. D., 1981: A method for determining the single scattering albedo of clouds through observation of the internal scattered radiation field. *J. Atmos. Sci.*, **38**, 2031-2044.

_____, 1983: Number of terms required in the Fourier expansion of the reflection function for optically thick atmospheres. *J. Quant. Spectrosc. Radiat. Transfer*, **30**, 143-161.

_____, 1987: Determination of the scaled optical thickness of clouds from reflected solar radiation measurements. *J. Atmos. Sci.*, **44**, 1734-1751.

_____, and Harshvardhan, 1986a: Comparative accuracy of selected multiple scattering approximations. *J. Atmos. Sci.*, **43**, 784-801.

_____, and _____, 1986b: Comparative accuracy of the albedo, transmission and absorption for selected radiative transfer approximations. NASA Ref. Pub. 1160, 41 pp.

_____, L. F. Radke, and P. V. Hobbs, 1990: Determination of the spectral absorption of solar radiation by marine stratocumulus clouds from airborne measurements within clouds. *J. Atmos. Sci.*, **47**, 894-907.

Lacis, A. A., and J. E. Hansen, 1974: A parameterization for the absorption of solar radiation in the Earth's atmosphere. *J. Atmos. Sci.*, **31**, 118-133.

Meador, W. E., and W. R. Weaver, 1980: Two– stream approximations to radiative transfer in planetary atmospheres: A unified description of existing methods and a new improvement. *J. Atmos. Sci.*, **37**, 630-643.

Sagan, C., and J.B. Pollack, 1967: Anisotropic nonconservative scattering and the clouds of Venus. *J. Geophys. Res.*, **72**, 469-477.

Shettle, E.P., and J.A. Weinman, 1970: The transfer of solar irradiance through inhomogeneous turbid atmospheres evaluated by Eddington's approximation. *J. Atmos. Sci.*, **27**, 1048-1055.

Slingo, A., 1989: A GCM parameterization for the shortwave radiative properties of water clouds. *J. Atmos. Sci.*, **46**, 1419-1427.

Stephens, G.L., 1988: Radiative transfer through arbitrarily shaped optical media. Parts I and II. *J. Atmos. Sci.*, **45**, 1818-1848.

Toon, O.B., C.P. McKay, T.P. Ackerman, and K. Santhanam, 1989: Rapid calculation of radiative heating rates and photodissociation rates in inhomogeneous multiple scattering atmospheres. *J. Geophys. Res.*, **94**, 16,287-16,301.

Twomey, S., 1976: Computations of the absorption of solar radiation by clouds. *J. Atmos. Sci.*, **33**, 1087-1091.

van de Hulst, H. C., 1968: Asymptotic fitting, a method for solving anisotropic transfer problems in thick layers. *J. Comput. Phys.*, **3**, 291-306.

_____, 1980: *Multiple Light Scattering, Tables, Formulas, and Applications*, Vols. 1 and 2. Academic Press, 739 pp.

Wiscombe, W.J., 1977: The delta-Eddington approximation for a vertically inhomogeneous atmosphere. NCAR Technical Note NCAR/TN -121 + STR, Boulder, CO., 66 pp. (NTIS PB 270618).

_____, and S. G. Warren, 1980: A model of the spectral albedo of snow. I: Pure snow. *J. Atmos. Sci.*, **37**, 2712-2733.

Zdunkowski, W.G., R.M. Welch, and G. Korb, 1980: An investigation of the structure of typical two-stream-methods for the calculation of solar fluxes and heating rates in clouds. *Contrib. Atmos. Phys.*, **53**, 147-166.

Table 1. Summary of γ_i coefficients in selected two-stream approximations.

Method	γ_1	γ_2	γ_3
Diffuse			
Eddington	$1/4\ [7-\omega_0(4+3g)]$	$-1/4\ [1-\omega_0(4-3g)]$	---
discrete ordinates	$\sqrt{3}/2[2-\omega_0(1+g)]$	$\sqrt{3}/2[\omega_0(1-g)]$	---
hemispheric mean	$2-\omega_0(1+g)$	$\omega_0(1-g)$	---
Integrated			
delta–Eddington	$1/4\ [7-\omega_0'(4+3g')]$	$-1/4\ [1-\omega_0'(4-3g')]$	$1/4(2-3g'\mu_0)$
Coakley-Chýlek (I)	$\{1-\omega_0[1-\beta(\mu_0)]\}/\mu_0$	$\omega_0\beta(\mu_0)/\mu_0$	$\beta(\mu_0)$

$\omega_0' = (1-g^2)\omega_0/(1-\omega_0 g^2)$

$g' = g/(1+g)$

FIGURE CAPTIONS

Fig. 1. Doubling computations of the (a) spherical albedo $\bar{r}(\tau_t, \omega_0)$, (b) global transmission $\bar{t}$ (τ_t, ω_0) and (c) global absorption $\bar{a}(\tau_t, \omega_0)$ as a function of optical thickness and single scattering albedo for the FWC phase function. The single scattering albedo scale is linear in the similarity parameter, defined by Eq. (4).

Fig. 2. Absolute accuracy of asymptotic theory, Eddington, discrete ordinates and hemispheric mean approximations to the spherical albedo, global transmission and global absorption as a function of optical thickness and single scattering albedo. The FWC phase function is assumed throughout.

Fig. 3. As in Fig. 2 except for relative accuracies (in percent).

Fig. 4. As in Fig. 2 but for the integrated delta-Eddington, two-point integrated delta-Eddington, integrated Coakley-Chýlek (I) and four-point integrated Coakley- Chýlek (I) approximations.

Fig. 5. As in Fig. 4 except for relative accuracies (in percent).

Fig. 6. The domain of validity of selected approximations to the diffuse radiative properties of cloud layers as a function of optical thickness (τ_t) and single scattering albedo (ω_0). The upper panels correspond to a relative accuracy of 1% and the lower panels to 5%. The single scattering albedo scale is linear in the similarity parameter. The FWC phase function is assumed throughout.

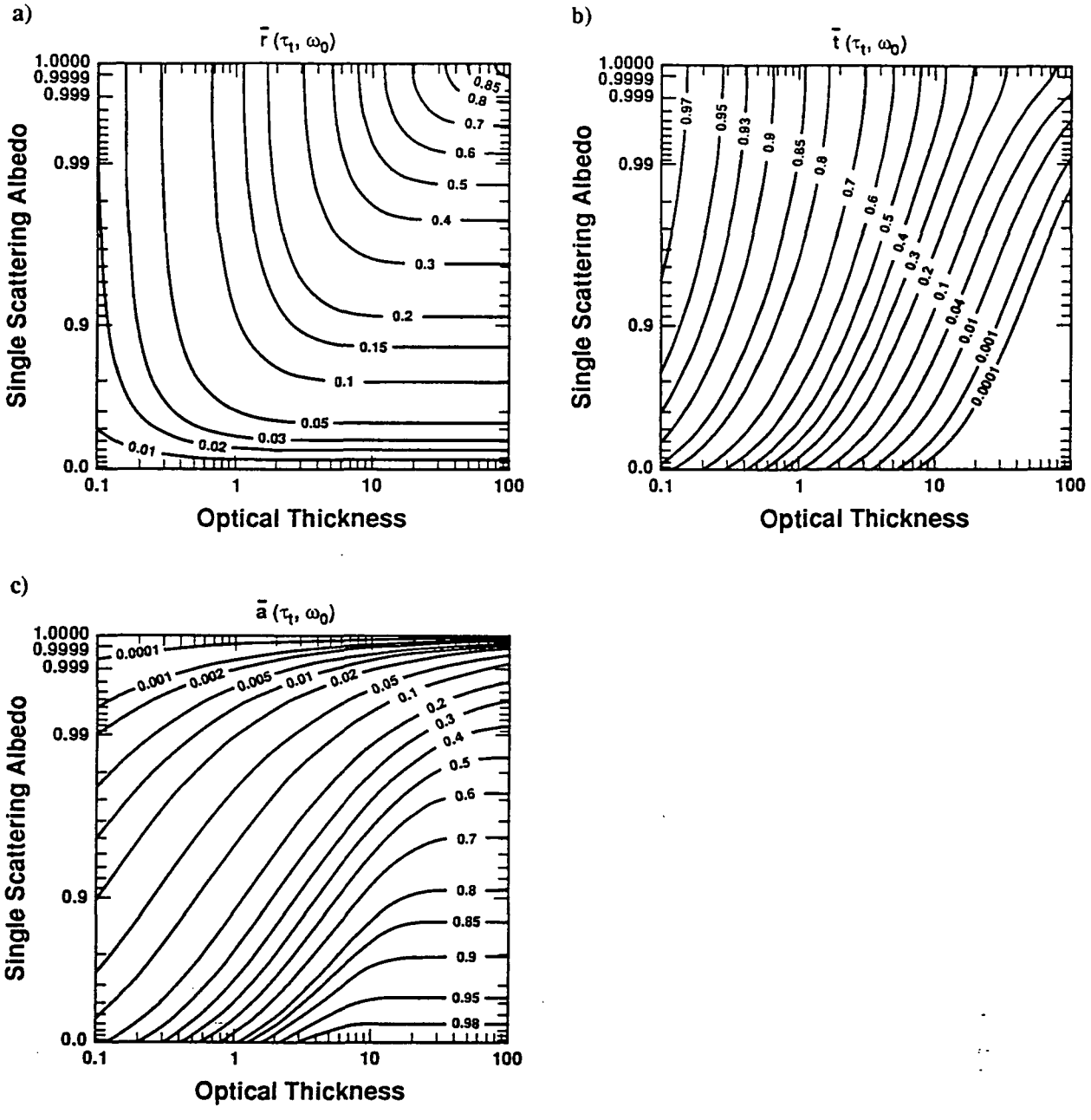
a)
$\bar{r}(\tau_t, \omega_0)$
Single Scattering Albedo
Optical Thickness
1.0000
0.9999
0.999
0.99
0.9
0.0
0.1
1
10
100
0.85
0.8
0.7
0.6
0.5
0.4
0.3
0.2
0.15
0.1
0.05
0.03
0.02
0.01
b)
$\bar{t}(\tau_t, \omega_0)$
Single Scattering Albedo
Optical Thickness
0.97
0.95
0.93
0.9
0.85
0.8
0.7
0.6
0.5
0.4
0.3
0.2
0.1
0.04
0.01
0.001
0.0001
c)
$\bar{a}(\tau_t, \omega_0)$
Single Scattering Albedo
Optical Thickness
0.0001
0.001
0.002
0.005
0.01
0.02
0.05
0.1
0.2
0.3
0.4
0.5
0.6
0.7
0.8
0.85
0.9
0.95
0.98

Figure 1

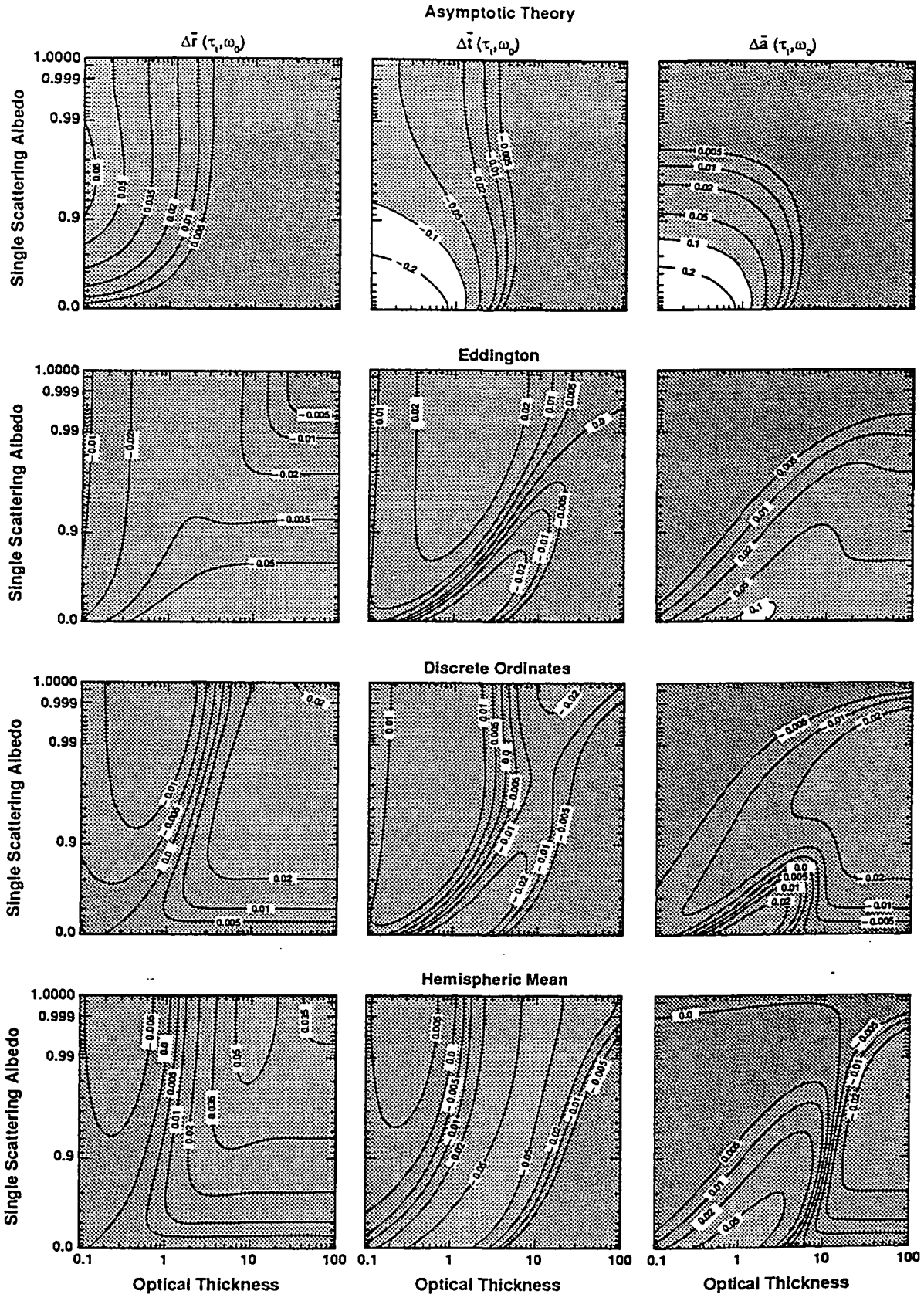
Asymptotic Theory
$\Delta\bar{r}\,(\tau_1,\omega_0)$
$\Delta\bar{t}\,(\tau_1,\omega_0)$
$\Delta\bar{a}\,(\tau_1,\omega_0)$
Eddington
Discrete Ordinates
Hemispheric Mean
Single Scattering Albedo
1.0000
0.999
0.99
0.9
0.0
0.1
1
10
100
Optical Thickness

Figure 2

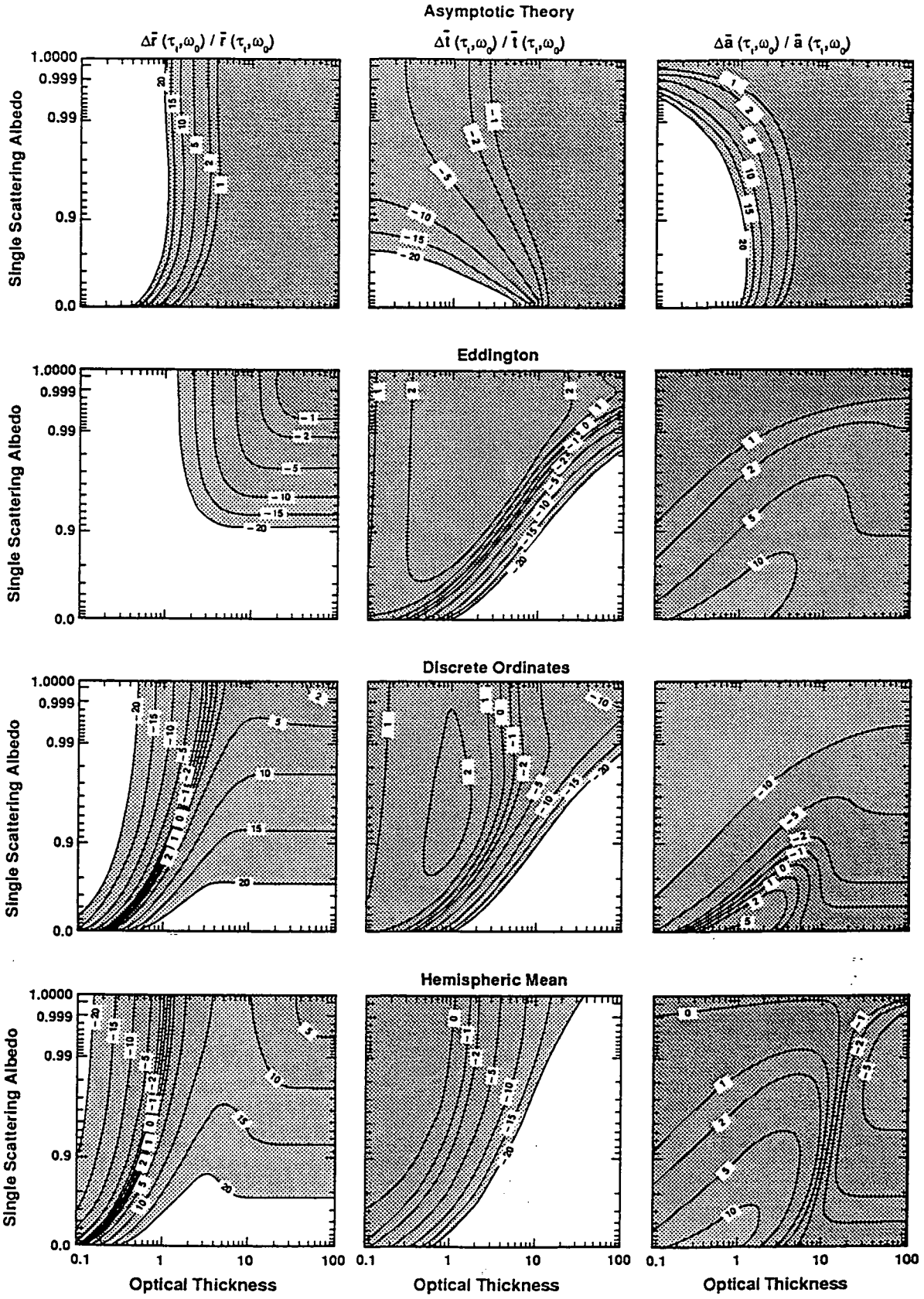
Asymptotic Theory
$\Delta\bar{r}\,(\tau_1,\omega_0)\,/\,\bar{r}\,(\tau_1,\omega_0)$
$\Delta\bar{t}\,(\tau_1,\omega_0)\,/\,\bar{t}\,(\tau_1,\omega_0)$
$\Delta\bar{a}\,(\tau_1,\omega_0)\,/\,\bar{a}\,(\tau_1,\omega_0)$
Eddington
Discrete Ordinates
Hemispheric Mean
Single Scattering Albedo
1.0000
0.999
0.99
0.9
0.0
0.1
1
10
100
Optical Thickness

Figure 3

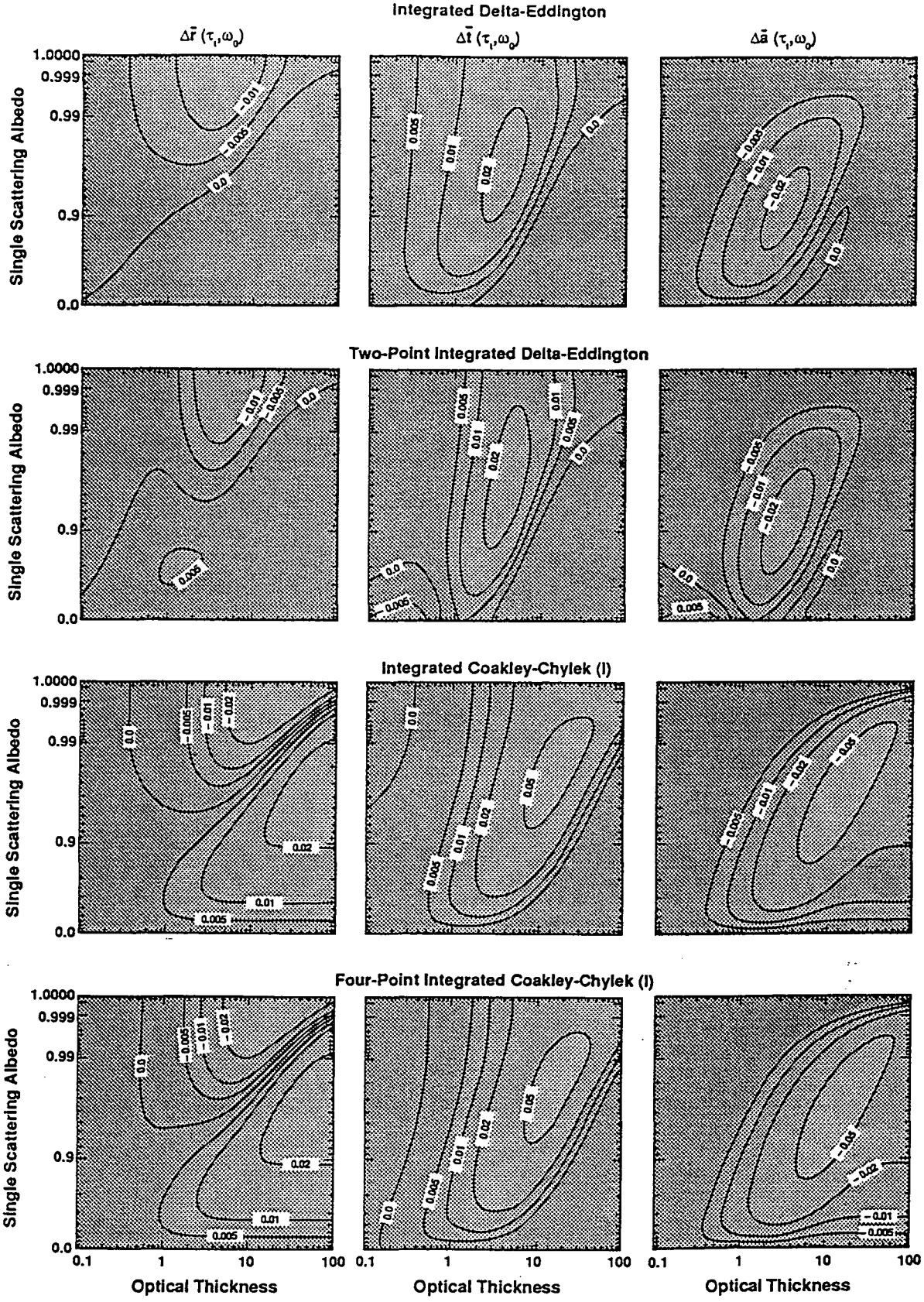
Integrated Delta-Eddington
$\Delta\bar{r}\ (\tau_t,\omega_o)$
$\Delta\bar{t}\ (\tau_t,\omega_o)$
$\Delta\bar{a}\ (\tau_t,\omega_o)$
Two-Point Integrated Delta-Eddington
Integrated Coakley-Chylek (I)
Four-Point Integrated Coakley-Chylek (I)
Single Scattering Albedo
1.0000
0.999
0.99
0.9
0.0
0.1
1
10
100
Optical Thickness

Figure 4

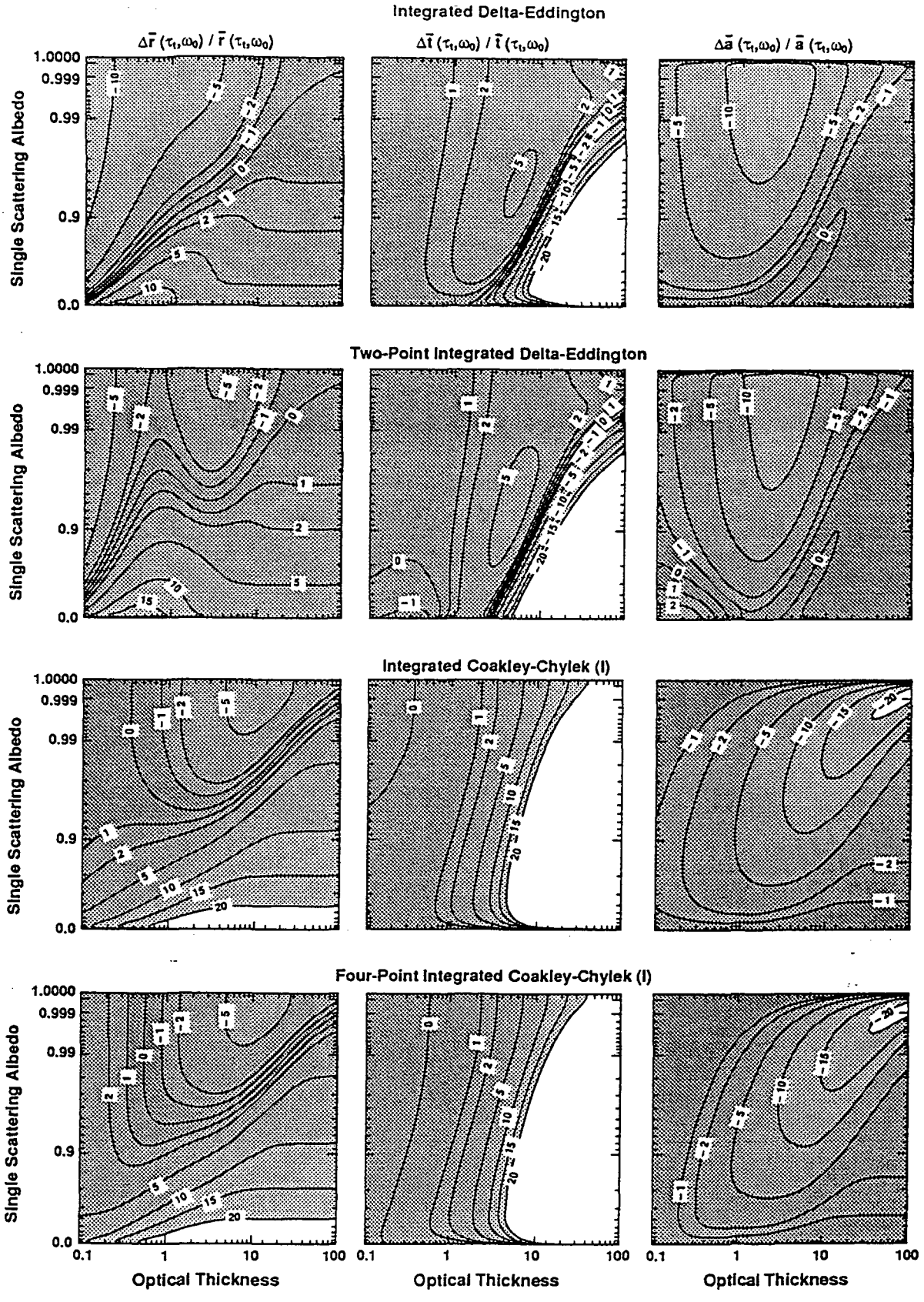
Integrated Delta-Eddington
$\Delta\bar{r}(\tau_t,\omega_0) / \bar{r}(\tau_t,\omega_0)$
$\Delta\bar{t}(\tau_t,\omega_0) / \bar{t}(\tau_t,\omega_0)$
$\Delta\bar{a}(\tau_t,\omega_0) / \bar{a}(\tau_t,\omega_0)$
Two-Point Integrated Delta-Eddington
Integrated Coakley-Chylek (I)
Four-Point Integrated Coakley-Chylek (I)
Single Scattering Albedo
1.0000
0.999
0.99
0.9
0.0
0.1
1
10
100
Optical Thickness

Figure 5

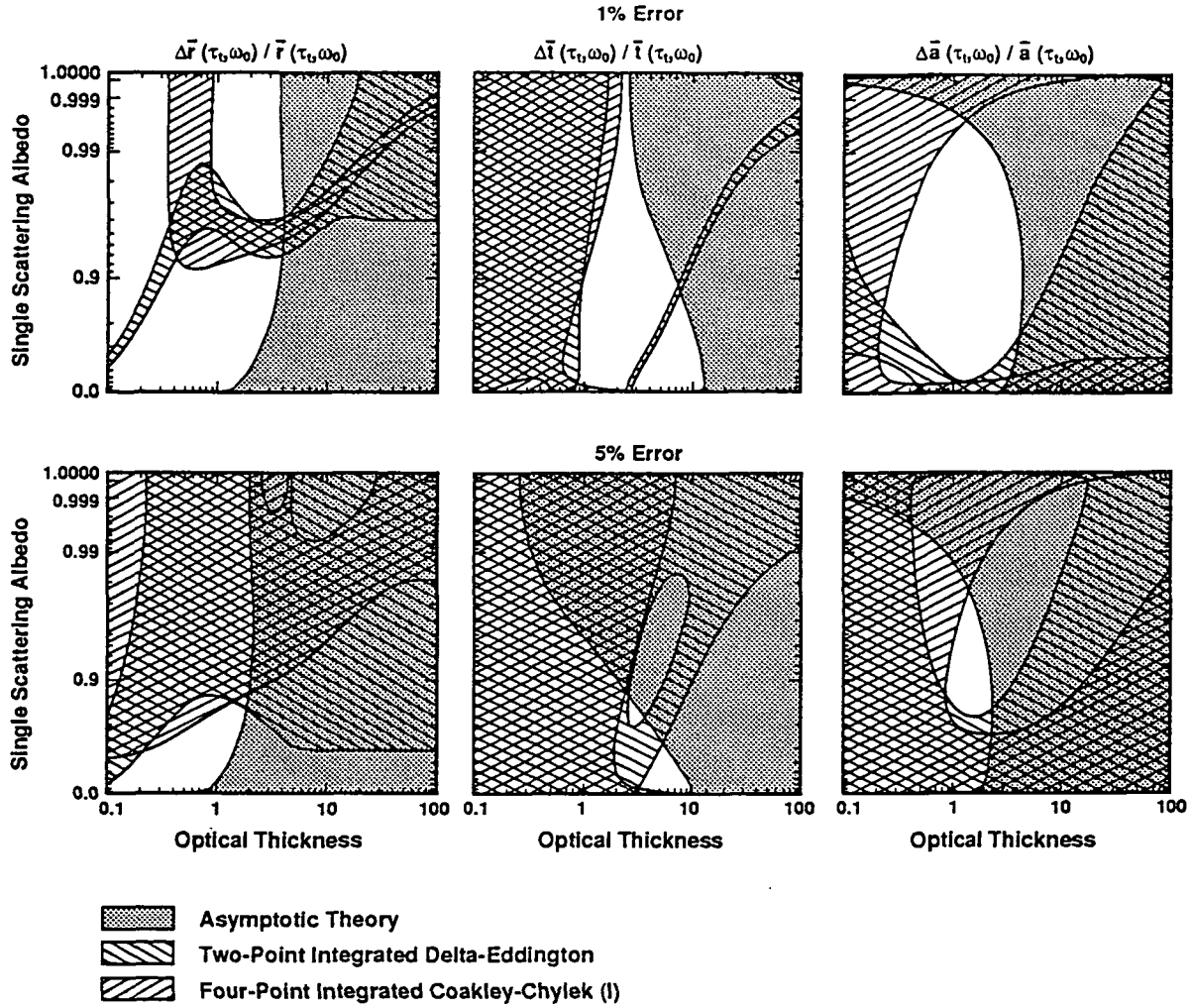
1% Error
$\Delta\bar{r}\,(\tau_t,\omega_0)\,/\,\bar{r}\,(\tau_t,\omega_0)$
$\Delta\bar{t}\,(\tau_t,\omega_0)\,/\,\bar{t}\,(\tau_t,\omega_0)$
$\Delta\bar{a}\,(\tau_t,\omega_0)\,/\,\bar{a}\,(\tau_t,\omega_0)$
Single Scattering Albedo
1.0000
0.999
0.99
0.9
0.0
5% Error
0.1
1
10
100
Optical Thickness
Asymptotic Theory
Two-Point Integrated Delta-Eddington
Four-Point Integrated Coakley-Chylek (I)

Figure 6